TECHNISCHE UNIVERSITÄT MÜNCHEN

LEHRSTUHL FÜR WINDENERGIE

# Master Thesis

## Rotor Design Procedure for a Drag Power Kite

André Frirdich
WE-MT-04-11

| | |
|---|---|
| Author: | André Frirdich |
| Registration number: | 03626450 |
| Professor: | Carlo L. Bottasso |
| Supervisors: | Filippo Campagnolo |
| | Florian Bauer (EI - EAL) |

Garching bei München, July 2019

## Statement of Authorship

I, André Frirdich, confirm that the work presented in this thesis has been performed and interpreted solely by myself except where explicitly identified to the contrary. All verbatim extracts have been distinguished by quotation marks, and all sources of information have been specifically acknowledged. I confirm that this work has not been submitted elsewhere in any other form for the fulfillment of any other degree or qualification.

Garching bei München, July 2019

# Abstract

A drag power kite is a flying wind turbine and consists of a rigid wing with small onboard turbines. The kite flies in crosswind trajectory on a figure eight flight path and is connected to a ground station by a high voltage tether. During crosswind flight the onboard turbines are used in generator mode to harvest energy. When the wind calms down, the turbines are used in motor mode to keep the kite airborne. Furthermore, the motor mode is used for vertical takeoff and landing like a multicopter. The rotors are designed to perform a continuous transition between motor and generator mode.

The evolutionary algorithm CMA-ES belongs to the class of genetic algorithms. In the present work CMA-ES is coupled with XRotor to find the global optimum of the annual energy yield by balancing the performance in motor and generator mode. A individual Weibull probability distribution for a certain wind speed is considered in the calculation of the annual energy yield. The multi-objective rotor design is regulated by CMA-ES with 18 free dimensioning parameters. Those are used to describe the rotor design by the chord distribution, the twist distribution, and the blade airfoils at three radial stations. The complete range of NACA 4 digit airfoils is calculated by XFoil and provided for CMA-ES.

The design procedure developed in the present work is applied for a $20\,kW$ kite configuration. The optimized rotor design reaches a maximum efficiency of $\eta_{max} = 86\,\%$ for a wind speed of $v_w = 12\,\frac{m}{s}$ and an average efficiency in generator mode of $\eta_{ave} = 83\,\%$ in the scope of the main wind speeds $7\,\frac{m}{s} < v_w < 20\,\frac{m}{s}$. The results are verified by using the blade element momentum theory. To increase the accuracy of the blade element momentum theory, the aerodynamic coefficients are calculated for every iteration by XFoil. The average deviation in the scope of the main wind speeds between XRotor and the blade element momentum theory is $4.5\,\%$. The annual energy yield of the $20\,kW$ kite configuration is $E_{el,yr} = 31,800\,\frac{kWh}{yr}$ and the power harvesting factor reaches a maximum value of $\zeta = 10$.



**Keywords:** XRotor, XFoil, airborne wind energy, drag power kites, evolutionary algorithm, CMA-ES, rotor design, blade element momentum theory, multi-objective optimization, aerodynamics.

| Symbol | Meaning |
|---|---|
| *Latin symbols* | |
| $A$ | Projected wing area [m$^2$] |
| $A_{rot}$ | Rotor disk area [m$^2$] |
| $C_L$ | Wing lift coefficient |
| $C_l$ | Blade airfoil lift coefficient |
| $C_{D,\Sigma}$ | System drag coefficient |
| $C_{D,k}$ | Kite drag coefficient |
| $C_{D,te}$ | Tether drag coefficient |
| $C_{D,tu}$ | Turbine drag coefficient |
| $C^*_{D,tu}$ | Optimal turbine drag coefficient |
| $C_d$ | Blade airfoil drag coefficient |
| $C_T$ | Thrust coefficient |
| $E_{el,yr}$ | Annual energy yield [kWh/yr] |
| $E$ | Lift-to-drag ratio |
| $F_{D,\Sigma}$ | System drag force [N] |
| $F_a$ | Resulting aerodynamic force [N] |
| $F_L$ | Wing lift force [N] |
| $F_{tu}$ | Turbine thrust force [N] |
| $F_g$ | Gravitational force [N] |
| $F_{te}$ | Tether force [N] |
| $K$ | Cost function |
| $Ma$ | Mach number |
| $N_b$ | Number of blades |
| $P_a$ | Aerodynamic power [kW] |
| $P^*_a$ | Optimal aerodynamic power [kW] |
| $P_w$ | Potential wind power [kW] |
| $P_{shaft}$ | Shaft power [kW] |
| $Q$ | Torque [N m] |
| $R_{tip}$ | Tip radius [m] |
| $Re$ | Reynolds number |
| $T$ | Thrust [N] |
| $a_{ind}$ | Axial induction factor |
| $a$ | Glide angle [°] |
| $m$ | Mass [kg] |
| $p(v_w)$ | Probability for a certain wind speed |
| $r$ | Radius [m] |
| $rpm$ | Rotational speed [1/min] |
| $v_w$ | Wind speed [m s$^{-1}$] |
| $v_a$ | True airspeed; inflow velocity [m s$^{-1}$] |
| $v_k$ | Kite speed [m s$^{-1}$] |
| $x_i$ | Free dimensioning parameters |

| **Symbol** | **Meaning** |
|---|---|
| $\underline{x}_i$ | Lower bounds |
| $\bar{x}_i$ | Upper bounds |
| *Greek symbols* | |
| $\alpha$ | Angle of attack [°] |
| $\delta$ | Penalties |
| $\zeta$ | Power harvesting factor |
| $\vartheta$ | Elevation angle [°] |
| $\eta$ | Efficiency |
| $\rho$ | Air density [kg/m$^3$] |
| $\varphi$ | Azimuth angle [°] |
| *Super-/subscripts* | |
| BEMT | Blade element momentum theory |
| HAWT | Horizontal axis wind turbine |
| DC | Design condition |
| XF | XFoil |
| XR | XRotor |
| ave | Average |
| gen | Generator mode |
| max | Maximum |
| min | Minimum |
| mot | Motor mode |
| rot | Rotor |
| tip | Blade tip |
| appx | Approximated |

# List of Figures

# List of Tables

# Contents

Chapter 1

# Introduction

## 1.1 Motivation

One of the central challenges of the 21th century is to stop the global warming and save our planet to be a livable place for all living things: humans, animals and nature. For accomplishing that aim, there are only a few decades left. The efforts towards the energy revolution need to be increased dramatically to achieve the $2\,^{\circ}C$ goal. The world's electricity demand is constantly growing and can only be covered by the use of fossil fuels or nuclear power. Renewable energy technologies are pointed to solve this problem. However, this sector is currently developing at a very slow pace, and the existing renewable energy technologies are not cost-effective enough.

Wind power has the potential to cover the world's electricity demand multiple times. Existing solutions to harvest wind energy are modern horizontal axis wind turbines (HAWTs), which have been optimized in the last two decades for maximum efficiency. Due to the increasing efficiency of the wind turbines, the wind energy market has constantly being growing in the last years and has turned out as a feasible solution for the energy revolution. However, modern wind turbines are ground-based solutions with high manufacturing and installation costs.

In contrast, airborne wind energy systems (AWESs) turned out to have the potential of passing the limits of modern HAWTs and to be the next generation renewables in the wind energy sector. AWESs need 10x less material, reach higher altitudes with steadier winds, and have a higher capacity factor and a lower $CO_2$-footprint than any other technology. Assuming that the technology of AWESs has a significant impact on the global climate, the present work was performed to contribute to the energy revolution.

Drag power kites are one of several concepts in the field of AWE. The kites fly in crosswind trajectory on a figure eight flight path and are connected to a ground station by a high voltage tether, while energy is produce by onboard turbines. The same turbines are used in reverse (motor mode) for vertical takeoff, landing and transition into crosswind flight. To increase the efficiency of a a drag power kite, customized rotors are necessary. Thus, the design procedure of such a customized rotor is the objective of the present work.

## 1.2 Procedure

The operation cycle of drag power kite rotors is divided into the following parts:

- Vertical takeoff like a multicopter (motor mode)
- Lift to operating altitude (motor mode)
- Transition into crosswind flight (motor mode)
- Energy generation during crosswind flight (generator mode)
- Transition into hover flight (motor mode)
- Vertical landing like a multicopter (motor mode)

The rotor faces multiple flight modes. To cover the scope of application, the rotor needs to be designed for a continuous transition between the two different flight modes, which are the motor mode and the generator mode. The ongoing transition between the two modes as well as the objective of a highly efficient rotor design can not be solved in an analytic way. Instead, numerical methods need to be applied in the form of the evolutionary algorithm CMA-ES. Therefore, a parametrization of the rotor design needs to be performed. Once the parametrization is given, constraints and the main design condition need to be implemented in the cost function of the evolutionary algorithm. The cost function is handled by penalties if the design condition or the constraints are violated. The given optimization setup needs to be coupled to the rotor design program XRotor.

Once the optimization yields a final rotor design, it needs to be verified by another independent rotor calculation. The BEMT will be used to perform a second independent calculation to verify the optimization. To increase the accuracy of the verification, the BEMT will be coupled to XFoil, a design program for isolated airfoils. The complete design procedure will be implemented in a MatLab environment and can be adapted to the kite system individually. The final rotor design procedure will be applied to a 20 kW kite design system developed by Bauer.

Chapter 2

# State of the Art

AWE is a relatively young technology and emerged with the publication of Miles Loyd "Crosswind Kite Power" in 1980 [25]. Loyd was inspired by George Pocock's book "The Aeropleustic Art or Navigation in the Air by the use of Kites, or Buoyant Sails", published over a century before in 1827 [27]. Loyd was the first to introduce the idea of crosswind kite power and formed the basis for all of the following works in this field. He derived a fundamental equation to describe the potential of crosswind flying kites by

$$P = \frac{2}{27}\rho v_w^3 A \frac{C_L^3}{C_D^2}, \tag{2.1}$$

explained in Sec. 3.1.1. Loyd's idea of crosswind kite power could not be established in the '80s and '90s as the interest in renewable and clean energy was vanishingly low. The oil crisis of the previous two decades had just passed and the oil industry boomed.

It took two decades to rediscover the technology of AWESs and Loyd's foundation. In 1997, the Delft University of Technology started investigation in lift power kites under the leadership of Prof. Wubbo Ockels, a Dutch astronaut. Only a few years later, in 2001, a German company called SkySails with the focus on flexible soft kites was founded, flying crosswind to support ship propulsions.

In 2006, a new competitor called Makani [26] dropped in with a Google investment. Thenceforward, Makani developed several prototypes, the first ones based on lift power, the later ones on drag power. To the present day, Makani is the leading competitor on the commercial side. In the following years several companies with focus on AWE were founded, e.g. Ampyx Power [2], EnerKite [14], or TwingTec [37].

The Delft University of Technology is still one of the leading scientific institutions in the field of AWE. Prof. Dr.-Ing. Roland Schmehl and his team Kitepower developed flexible lift power kites [23], supported by Prof. Dr. rer. nat. Moritz Diehl from the University of Freiburg [38]. Moreover, Schmehl published the book "Airborne Wind Energy" [1] together with Uwe Ahrens and Moritz Diehl. Several publications regarding AWE are summarized in this work.

Florian Bauer, PhD candidate at the Chair of Electrical Drive Systems and Power Electronics at the Technical University of Munich, analyzed the current AWE sector and, based on the obtained data, performed a multi-objective optimization for drag power kites [4]. One result of Bauer's investigations is the prelimary design of a 20 kW drag power kite.

The present work is embedded in Bauer's multi-objective optimization of drag power kites. The aim is to develop a general rotor design procedure for drag power kites, exemplarily applied to the 20 kW kite system of Bauer. As the AWE technology still is in an early stage, no works are published regarding the rotor design procedure for a drag power kite.

A common used rotor for an airplane propulsion is coupled to a motor and inserts power into the airflow passing the rotor. This results in a thrust force to compensate the drag of the airplane and keep the airplane airborne [30].

A common used rotor for a wind turbine is coupled to a generator and extracts power out of the airflow passing the rotor. This results in shaft power, which is transferred into electrical power by the generator [7].

The design procedures for airplane propellers or for wind turbines are, in a simplified perspective, single-objective design procedures. A rotor for a drag power kite needs to combine the motor mode of the airplane propeller with the generator mode of a wind turbine described above. Hence, classical design procedures can not be applied to the rotor design for a drag power kite, so that a new approach needs to be developed to solve the multi-objective rotor design.

Chapter 3

# Fundamentals

## 3.1 Crosswind Kite Power

In the current wind energy sector ground-based three bladed HAWTs are established as the standard model to harvest wind energy. In contrast to HAWTs, in the sector of AWESs, kites fly in crosswind trajectory and replace the supporting structure, such as the tower and the nacelle of a HAWT, by a tether. The tether is necessary to keep the kite on a figure eight or circle flight path by increasing the relative velocity (true airspeed) between the kite and the ground to a multiple of the local wind speed. The kinematic energy of the mass of air passing the kite keeps the kite airborne and has the potential for large-scale energy production. The prime benefits of crosswind kite power are the following [1]:

- Kites reach stronger and steadier winds in higher altitudes compared to HAWTs.
- Material needed for a kite is 10x less than the material needed for a comparable HAWT.

Crosswind kite power can be divided in two physical approaches to harvest wind energy [25]:

**A Lift Power Kite** flies in crosswind trajectory and produces lift due to aerodynamic forces. A small amount of the lift force is used to compensate kite and tether drag and to keep the kite airborne. The excessive amount of the lift force serves to increase the tether strength and therefore roll-up a tether connected ground-based electric generator, which is called the energy harvesting reel-out phase. As the tether length and therefore the reel-out phase are limited, a periodic cycle is needed. When reaching the maximum tether length, the kite needs to produce less lift to start the retraction of the tether, called the reel-in phase. The combination of the reel-out and the reel-in phase is called pumping or Yo-Yo mode. Commonly, surf kites are used for lift power kites, because of their flexibility, low mass and the simplified fly control. Rigid kites are rarely used as lift power kites due to harder flight control and a more complex starting and landing procedure. However, higher lift coefficients can be achieved with them.

**A Drag Power Kite** has a fixed tether length and continuously generates power without any pumping mode. Comparable to lift power kites, a small amount of the lift force is used to compensate kite and tether drag and to keep the kite airborne. In contrast to lift power kites, the excessive amount of the lift force gets in balance with an additional drag force produced by the onboard turbines. The aim is to reach high true airspeeds to increase the turbine drag and therefore the power output. As shown in Fig. 3.1, a drag power kite consists of a rigid airfoil with several installed powertrains on top. Those powertrains work either as a propeller-motor unity for vertical takeoff / landing and transition into crosswind flight or as a rotor-generator unity for energy production in figure eight crosswind flight. To keep the kite on the figure eight flight path and to transmit the onboard generated electricity, the kite is connected to the ground station via a high voltage tether.

Further information about AWE and crosswind kite power can be found in [1, 8, 15, 25].

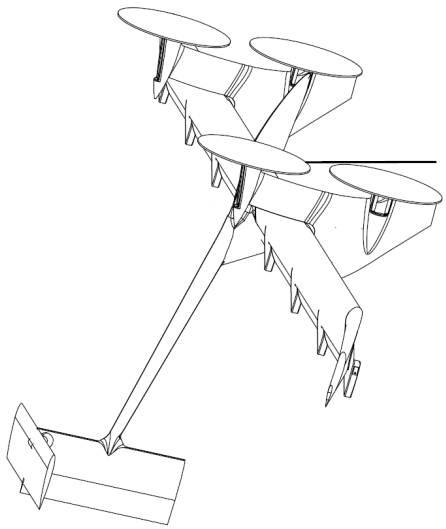

Figure 3.1: Model of a drag power kite.[1]

The following sections describe a extended version of the crosswind kite power concept [5, Chapter 2] originally introduced by Loyd in 1980 [25].

### 3.1.1 Drag Power Kite Kinematics

According to Bauer the following assumptions are made for the kite kinematics model:

1. *"Gravitational and inertial forces are small compared to aerodynamic forces."*[5, p. 3]
2. *"The tether is straight, so that, in combination with Assumption 1, aerodynamic force $F_a$ and tether force $F_{te}$ are in balance (...)."*[5, p. 3]
3. *"The kite does not fly through its own wake (...)."*[5, p. 3]

Above some minimum true airspeed the aerodynamic forces are dominant and assumption 1 and 2 are valid. Furthermore, assumption 3 is valid as the kite flies in large circles or figure eights and passes a large air mass [1, Chapter 28]. In Fig. 3.2 the force equilibrium of a drag power kite is shown. By means of Fig. 3.2 following equation can be extraceted:

$$\frac{\cos(\varphi)\cos(\vartheta)v_w}{v_a} = \sin(a) = \frac{F_{D,\Sigma}}{F_a}. \tag{3.1}$$

Eq. 3.1 is a trigonometric relation between the wind speed $v_w$, the true air speed $v_a$, the glide angle $a$ and the aerodynamic forces defined by

$$F_L = \frac{1}{2}\rho v_a^2 A C_L, \tag{3.2}$$

$$F_{D,\Sigma} = \frac{1}{2}\rho v_a^2 A C_{D,\Sigma} \quad \text{and} \tag{3.3}$$

$$F_a = \sqrt{F_L^2 + F_{D,\Sigma}^2}. \tag{3.4}$$

[1] Source: Bauer [1]

$A$ is the projected wing area, $\rho$ the air density, $F_L$ and $F_{D,\Sigma}$ the total lift and drag force with the corresponding lift and drag coefficients $C_L$ and $C_{D,\Sigma}$. $C_{D,\Sigma}$ is divided in a drag coefficient for the kite $C_{D,k}$, the tether $C_{D,te}$ and the turbine $C_{D,tu}$ by

$$C_{D,\Sigma} = C_{D,k} + C_{D,te} + C_{D,tu} \tag{3.5}$$

with

$$C_{D,eq} = C_{D,k} + C_{D,te}. \tag{3.6}$$

The combination of Eq. 3.1 with 3.2 and 3.4 leads to

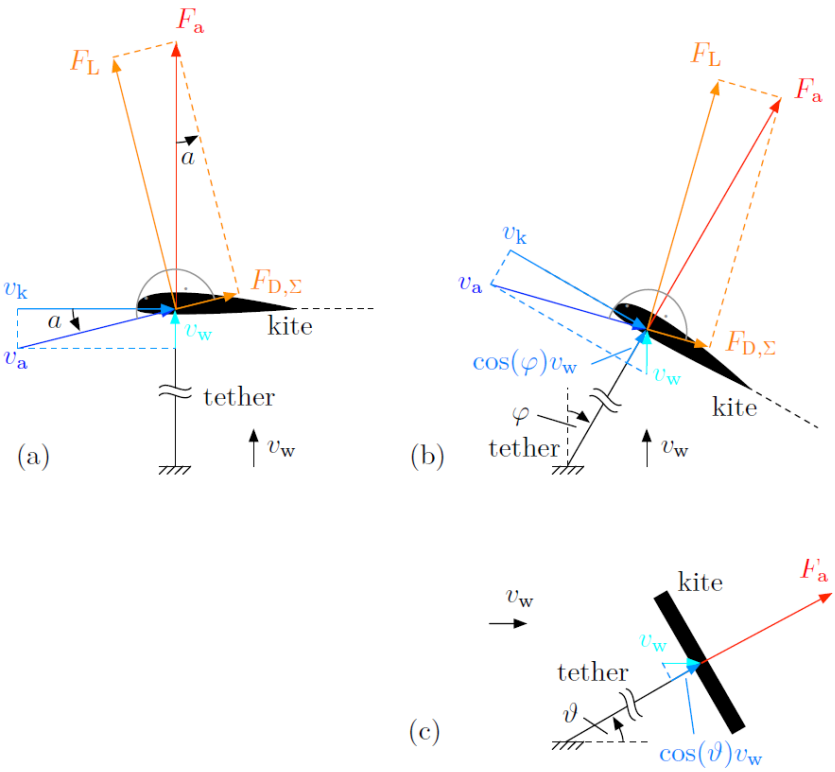


Figure 3.2: Force equilibrium of a drag power kite in crosswind flight with the lift force $F_L$, the total drag force $F_{D,\Sigma}$, the resulting aerodynamic force $F_a$, the wind velocity $v_w$, the kite velocity $v_k$, the resulting aerodynamic velocity $v_a$, the azimuth angle $\varphi$, and the elevation angle $\vartheta$.[2]

$$v_a = \cos(\varphi)\cos(\vartheta)v_w \frac{\sqrt{C_L^2 + C_{D,\Sigma}^2}}{C_{D,\Sigma}}. \tag{3.7}$$

Similar to the aerodynamic forces in Eq. 3.2 and 3.4 the turbines thrust force is defined by

$$F_{tu} = \frac{1}{2}\rho v_a^2 A C_{D,tu}. \tag{3.8}$$

With the turbine thrust force Eq. 3.8, the true airspeed Eq. 3.7, the azimuth angle $\varphi$, and the elevation angle $\vartheta$, the aerodynamic power $P_a$ is given by

$$\begin{aligned} P_a &= v_a F_{tu} \\ &= \frac{1}{2}\rho \cos^3(\varphi)\cos^3(\vartheta) v_w^3 A \frac{\sqrt{C_L^2 + (C_{D,eq} + C_{D,tu})^2}^3}{(C_{D,eq} + C_{D,tu})^3} C_{D,tu}. \end{aligned} \tag{3.9}$$

[2]Source: Bauer [5]

### 3.1.2 Optimal Rotor Design Condition

The kinematic model of the kite in the previous section yields Eq. 3.9 for the aerodynamic power. The first step of the rotor design procedure is to determine the optimal values for the turbine drag coefficient $C_{D,tu}$ by differentiation of Eq. 3.9 w.r.t. $C_{D,tu}$ [25], which leads to an optimal turbine drag coefficient

$$C^*_{D,tu} = \frac{1}{2} C_{D,eq}. \tag{3.10}$$

In this case, the optimal aerodynamic power becomes

$$P^*_a = \frac{4}{27}\frac{1}{2}\rho \cos^3(\varphi)\cos^3(\vartheta) v_w^3 \frac{C_L^3}{C_{D,eq}^2}. \tag{3.11}$$

Within these calculations and for all further calculations a assumption in aerodynamics for efficient airfoils is:

4. *"The effective lift coefficient is much higher than the effective drag coefficient sum (...)"*[5, p. 3]

and therefore

$$\sqrt{C_L^2 + C_{D,\Sigma}^2} \approx C_L. \tag{3.12}$$

Detailed definitions of the lift and drag coefficients of the kite and the tether can be found in [5].

### 3.1.3 Power Curve

The power curve of a drag power kite is shown in Fig. 3.3. According to Lind [1, Chapter 28] the power curve is distinguished in four main regions. The fifth region just serves to illustrate the cut-out wind speed with power output zero.

#### Region I

The first region is split in two fields:

- **Pre-zero-crossing** with a defined negative power output for motor mode.
- **Post-zero-crossing** with a defined positive power output for generator mode.

Because of the power consumption in the pre-zero-crossing field, the kite would not start at those low wind speeds and therefore this field is handled as a constraint in the rotor optimization procedure. Furthermore, in the complete region I, except at the transition point to region II, the kite is not working at the optimal power output. That means that the turbine drag coefficient is lower than the optimal turbine drag coefficient, given in Eq. 3.10. The local condition in region I is to ensure a constant minimum true airspeed $v_{a,min}$ to keep the kite airborne and to satisfy assumption 1 and 2 in Sec. 3.1.1. Conforming with Bauer [5], $v_{a,min}$ can be derived with trigonometric relations between the aerodynamic lift force $F_a$, the tether force $F_{te}$ and the gravitational force $F_g$ shown in Fig. 3.4, with

$$v_{a,min} = \sqrt{\frac{mg}{\frac{1}{2}\rho A C_L}\frac{\cos(\vartheta)}{\sin(\psi_{w,max})}}. \tag{3.13}$$

[3]Source: Lind [1, Chapter 28]
[4]Source: Bauer [5]

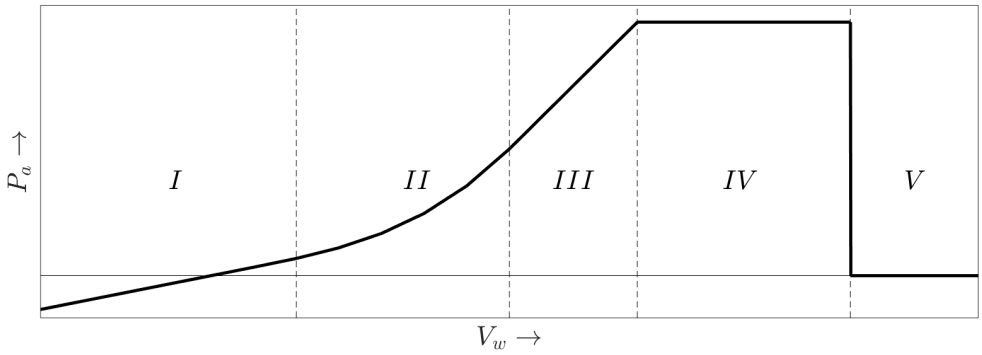


Figure 3.3: Optimal power curve of a drag power kite distinguished in essential five regions, where different power behavior depending on the wind speed can be detected.. Aerodynamic power $P_a$ is plotted over the wind speed $v_w$. Linear region $I$ is characterized by the minimum true airspeed $v_{a,min}$, Region $II$ by the optimal power output, Region $III$ by a maximum tether force $F_{te,max}$, Region $IV$ by the capacity of the generator and Region $V$ by the cut-out wind speed.[3]

With Eq. 3.12 in mind, inserting and 3.6 in 3.7 and in 3.9 leads to

$$C_{D,tu} = \frac{\cos(\varphi)\cos(\vartheta)v_w}{v_{a,min}} C_L - C_{D,eq} \tag{3.14}$$

and

$$P_{a,I} = \frac{1}{2}\rho A v_{a,min}^3 \left( \frac{\cos(\varphi)\cos(\vartheta)v_w}{v_{a,min}} C_L - C_{D,eq} \right) \tag{3.15}$$

Setting $P_{a,I} = 0$ gives the cut-in wind speed.

$$v_{w,cut-in} = \frac{v_{a,min}}{\cos(\varphi)\cos(\vartheta)} \frac{C_{D,eq}}{C_L}. \tag{3.16}$$

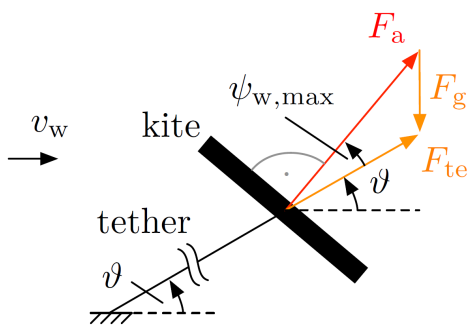


Figure 3.4: Back view in flight trajectory of a drag power kite. With the tether force $F_{te}$, the gravitational force $F_g$, the resulting aerodynamic force $F_a$, the wind velocity $v_w$, and the elevation angle $\vartheta$.[4]

### Region II

In Region II no limitations are given and the equations for the optimal turbine drag coefficient 3.10 and the optimal power output 3.11 can be applied. Therefore, the transition point between region I and II is given by setting $v_a = v_{a,min}$ and $C_{D,tu} = C^*_{D,tu}$ in Eq. 3.7, which leads to

$$v_{w,I\rightarrow II} = \frac{v_{a,min}}{\cos(\varphi)\cos(\vartheta)} \frac{\frac{3}{2} C_{D,eq}}{C_L}. \tag{3.17}$$

The wind shear is not taken into account in all explanations during the master project, which is a simplification of reality. More detailed information regarding to the wind shear can be found in [5].

### Region III

Region III is increasing linear and limited by the maximum tension in the tether, which depends on the tether properties and the safety factor. According to [1, Chapter 28], the tether force $F_{te}$ can be approximated with

$$F_{te} = \frac{1}{2}\rho A v_a^2 C_L. \tag{3.18}$$

According to [1, Chapter 28], setting $F_{te} = F_{te,max}$ and inserting the calculated air speed $v_{a,max}$ in Eq. 3.7 and 3.9 by neglecting the azimuth and elevation angle leads to

$$P_{a,III} = F_{te,max} \left( v_w - \sqrt{\frac{2F_{te,max}}{\rho A} \frac{C^2_{D,\Sigma}}{C^3_L}} \right). \tag{3.19}$$

### Region IV

As well as the tether force, the power output is limited by the maximum generator capacity in region IV, $P_{a,IV} = P_{max}$. Inserting $P_{max}$ in Eq. 3.19 gives

$$v_w = \frac{P_{max}}{T_{max}} \sqrt{\frac{2F_{te,max}}{\rho A} \frac{C^2_{D,\Sigma}}{C^3_L}}. \tag{3.20}$$

### 3.1.4 Power Harvesting Factor and Rotor Efficiency

The total amount of energy in the wind is defined by

$$P^*_w = \frac{1}{2}\rho v_w^3 A. \tag{3.21}$$

The aerodynamic power divided by the energy in the wind [1, Chapter 28] leads to the power harvesting factor

$$\begin{aligned} \zeta &= \frac{P_a}{P_w} \\ &= \frac{4}{27}\rho \cos^3(\varphi)\cos^3(\vartheta) \frac{C^3_L}{C^2_{D,eq}}. \end{aligned} \tag{3.22}$$

Glauert defined the efficiency of a propeller as the relation between the aerodynamic power $P_a$ and the mechanical shaft power $P_{shaft}$ [13, Devision L]. Therefore, the efficiency in motor and generator mode is defined as

$$\eta_{mot} = \eta^{-1}_{gen} = \frac{P_a}{P_{shaft}} = \frac{F_{tu}\, v_a}{\Omega\, Q}, \tag{3.23}$$

with $\Omega$ being the angular velocity of the turbine shaft and $Q$ the acting torque.

### 3.1.5 Energy Yield

Aligned with [5], [7, Chapter 3.16] and [29, Chapter 6.7.1], the annual energy yield is given with

$$E_{el,yr} = \frac{8,760\,h}{1\,yr} \int_0^\infty p(v_w) P_{shaft+}(v_w)\, dv_w. \tag{3.24}$$

In the calculation of the annual energy yield, only the positive shaft power values $P_{shaft+}$ are considered, it is non-economical to operate the kite when power is consumed. The probability $p(v_w)$ of a certain wind speed depends on the location where the kite is installed. It is describe by a Weibull distribution based on local wind measurements.

## 3.2 XRotor

XRotor is a design and analysis software written by Drela at the Massachusetts Institute of Technology [10]. The user guide of XRotor can be found in [12]. Drela's software is based on the lifting line theory published 1919 by Betz and Prandtl [28] and was reformulated 1929 by Goldstein [17], 1948 by Theodorsen [36] and 1983 by Larrabee [24]. The lifting line theory was compared to experimental data of a SR-2 propeller by Schulten in [31].

The code of XRotor iteratively solves the equations for the bound vortex and the discrete line vortices of the helicoidal wake. To calculate the vortices and therefore the induced velocities, the airfoil properties of the used profiles are needed. As well as the BEMT [16], the lifting line theory separates the rotor blade in radial sections. Every section has different local flow velocities and different geometric dimensions. Therefore, the aerodynamic airfoil parameters are changing for each section and can be supplied by the panel method software XFoil, developed by Drela as well [11]. With the given airfoil parameters XRotor uses a linear $C_l - \alpha$ and a quadratic $C_d - C_l$ curve and includes a stall prediction [12]. Furthermore, a Reynolds and Mach scaling [12] as well as the Prandtl tip loss model [28] is used. In contrast to the BEMT, XRotor does not neglect the influence of radial velocities, which means that the induced velocities of neighbouring sections in radial direction are coupled to each other. Due to a higher resolution of the flow, the computational efforts of the lifting line theory increases in comparison to the BEMT, but are still in the order of seconds. XRotor has been applied in several publishments [6, 9, 20, 21, 32, 34, 39].

## 3.3 Evolutionary Algorithm: CMA-ES

The Covariance Matrix Adaptation Evolution Strategy (CMA-ES) belongs to the class of genetic algorithm and is a stochastic numerical black box optimization. A sketch of the CMA-Es inputs and outputs is presented in Fig. 3.5. CMA-ES applies for non-convex and non-linear problems. The input values are defined as a vector $\vec{x}$ the output values as a function of the input values $f(\vec{x})$.

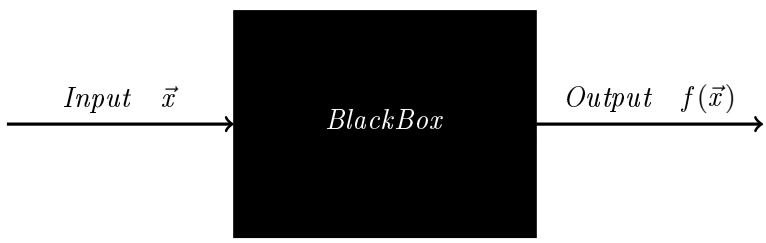


Figure 3.5: CMA-ES optimization problem illustrated as a black box with the input values $\vec{x}$ and the output values $f(\vec{x})$.

In our case, the rotor calculation is inside the black box and CMA-ES just reacts on the input by observing the output. For getting the global optimum, heuristic rules of the recent generation are coupled to the feedback of earlier populations. The run time towards the global optimum is reduced by simultaneous selection and variation of non-separable variables. CMA-ES does not make any efforts of calculating gradients and a Jacobian matrix, which extends the application to non-continuous problems and reduces the run time further. The broad application area, the off-the-shelf availability, and the simple setup of CMA-ES established the algorithm as a standard model in numerical optimization. A list of publishments using CMA-ES and detailed explanations can be found in [3, 18, 19, 35].

Chapter 4

# Rotor Design Procedure

The first section contains the results of a small-scale drag power kite design performed by Bauer with an multidisciplinary optimization algorithm [4]. The complete rotor design procedure in the present work is embedded in the work of Bauer. The next section describes the parametrization of a rotor blade to define the parameters, which are regulated by CMA-ES, in the following called free dimensioning parameters. The coupling of the evolutionary algorithm CMA-ES with XRotor and the optimization setup therein is explained in the following section. In the last section, a validation method for the optimized rotor is introduced.

## 4.1 Design Condition - Predefined Power Curve

As shown in Fig. 3.3, a power curve of a drag power kite has four main regions. For each region the equations given in Sec. 3.1.3 can be applied to calculate the aerodynamic power $P_a$ per rotor and the true airspeed $v_a$ depending on the wind speed $v_w$ as shown in Fig. 4.1a.

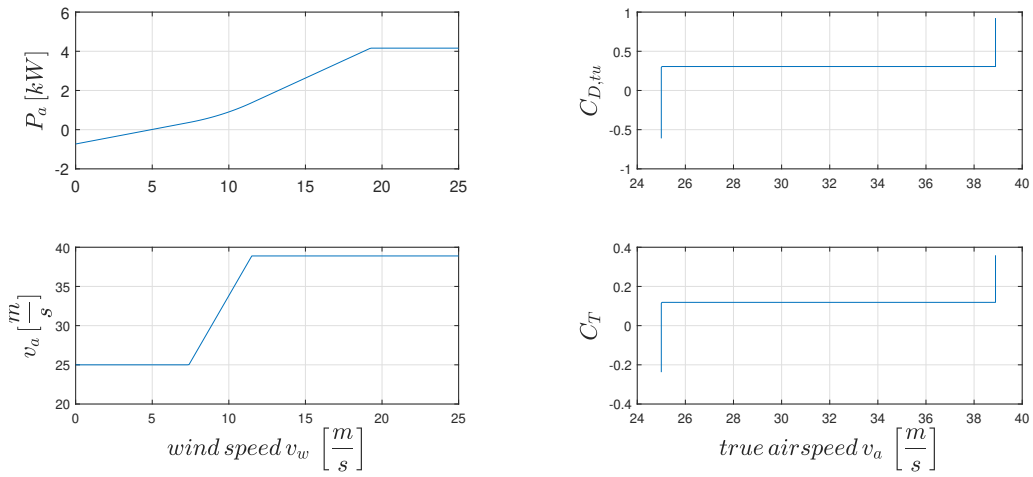


(a) (b)

Figure 4.1: Initial power curve of a targeted small-scale drag power kite. Fig. 4.1a shows the aerodynamic power $P_a$ and the true airspeed $v_a$ plotted over the wind speed $v_w$. Fig. 4.1b shows the turbine drag coefficient $C_{D,tu}$ and the rotor thrust coefficient $C_T$ plotted over the true airspeed $v_a$.

The obtained curve for the true airspeed $v_a$ is characterized by two constant values, $v_{a,min}$ and $v_{a,max}$, and a linear increase between those values. They are caused by the minimum tether force to keep the kite airborne, and the maximum tether force within a safety factor. Once the aerodynamic power and the true airspeed are given, the needed turbine thrust $F_{tu}$ can be calculated with Eq. 3.9.

At this point, we need to introduce two different coefficients: the turbine drag coefficient

$C_{D,tu}$ and the rotor thrust coefficient $C_T$ plotted in Fig. 4.1b over the true airspeed $v_a$. Both coefficients are based on the turbine thrust force $F_{tu}$, which is the same as the rotor thrust force $T$ and therefore called rotor thrust from this point on. The nondimensionalization of the rotor thrust with the projected wing area $A$ and the wind speed $v_w$ according to Eq. 3.8 is defined as the turbine drag coefficient $C_{D,tu}$. Conversely, the nondimensionalization with the rotor disk area $A_{rot} = \pi R_{tip}^2$ and the true airspeed $v_a$ is defined as the rotor thrust coefficient $C_T$ with

$$C_T = \frac{T}{\frac{1}{2}\rho v_a^2}. \tag{4.1}$$

The first step in the rotor design procedure for a drag power kite is to know the thrust the rotor has to provide, to satisfy the predefined power curve (Fig. 4.2).

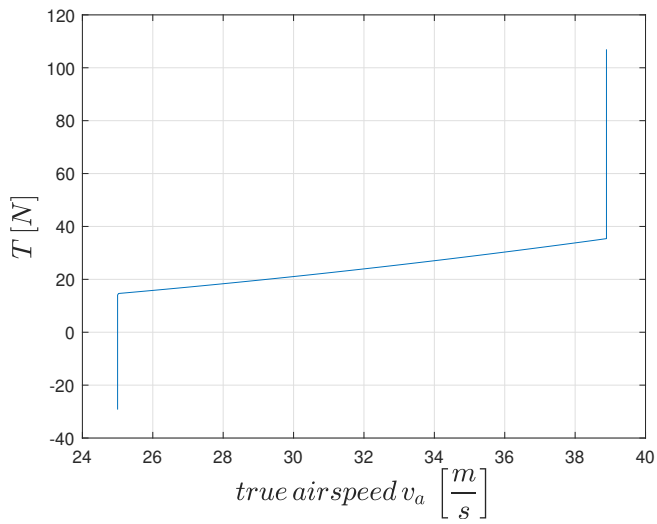


Figure 4.2: Rotor thrust resulting from a predefined power curve. With the thrust $T$ plotted over the true airspeed $v_a$.

As long as the kite is operating in motor mode, the rotor thrust is negative and energy is consumed. In generator mode the thrustas well as the power output gets positive, and therefore energy is produced.

## 4.2 Parametrization

XRotor is able to run arbitrary rotor designs. The main design options for an arbitrary rotor are the twist and chord distribution and the camber and thickness of the airfoils used along the radius of the blade. Fig. 4.3 shows the used parametrization in this project. In total, 18 dimensioning parameters are used to describe the arbitrary rotor design. Upper-case letters describe coordinates in the x y plane, lower-case letters are the dimensionising parameters.

The chord distribution is approximated by 5 dimensioning parameters with two curves. The first curve describes the chord distribution in the hub region. The first dimensioning parameter $x_1$ is defined by the maximum chord value

$$X_1 = x_1 R_{tip} \quad \text{with} \quad x_1 < 0.3. \tag{4.2}$$

The circumference of a circle at a given radius is

$$C = 2\pi r. \tag{4.3}$$

Eq. 4.3 divided by the number of blades $N_b$ and multiplied by the second dimensioning parameter $x_2$ leads to the chord distribution in the hub region

$$chord_I(r) = \frac{2\pi r}{N_b} x_2 \quad \text{with} \quad x_2 < 1 \quad \text{and} \quad chord_{hub}(r) \leq X_1. \tag{4.4}$$

The dimensioning parameter $x_2$ can be described as a factor that limits the disk area in the hub region, which is covered by the blades. The result is a linear curve in the hub region, where $X_1$ and $X_2$ are the values of the point coordinates, calculated by combining Eq. 4.2 and 4.4. The last three parameters of the chord distribution are given by

$$X_3 = x_3 \cdot X_1 \quad \text{with} \quad x_2 < 1, \tag{4.5}$$

$$X_5 = x_5 \cdot X_3 \quad \text{with} \quad x_5 < 1 \tag{4.6}$$

and

$$\frac{1}{4} R_{tip} < x_4 < \frac{3}{4} R_{tip} \tag{4.7}$$

In the end, three data-points are given and a quadratic curve with

$$chord_{II}(r) = ar^2 + br + c \tag{4.8}$$

can be calculated to complete the chord distribution. The twist distribution is parameterized in the same way as $chord_{II}(r)$. The values $X_6$ and $X_9$ are located at the hub and the tip of the blade. Once the twist and chord distributions are known, the blade can be split in various radial sections $N_s$, and for each section the twist and chord can be calculated.

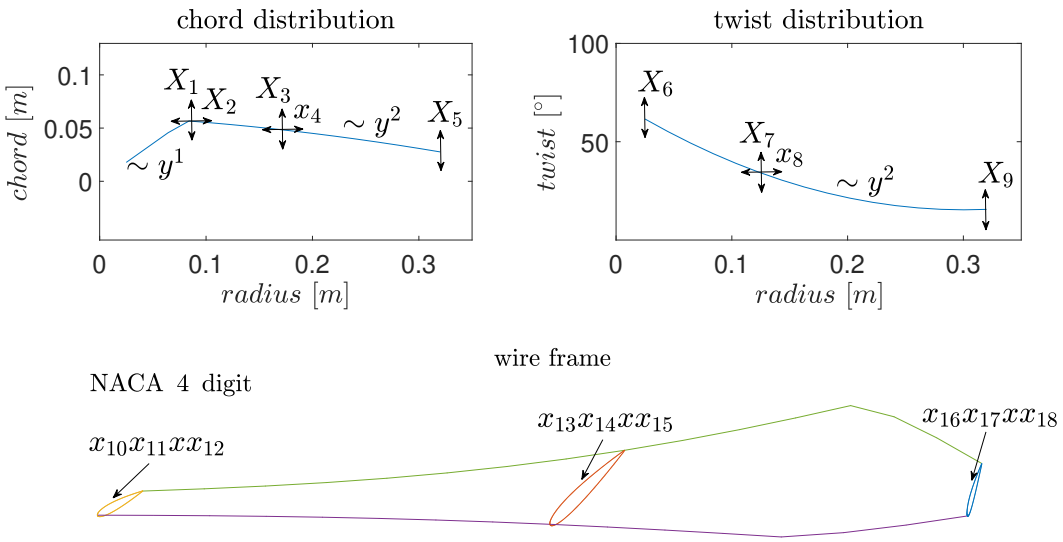


Figure 4.3: Rotor parametrization defined by five free dimensiong parameters for the chord distribution $x_{1-5}$, four for the twist distribution $x_{6-9}$ and nine for the blade shape $x_{10-18}$. The corresponding upper-case letters $X_i$ are discrete x- or y-coordinates resulting from the lower-case free dimensioning parameters $x_i$.

NACA 4 digit airfoils are used to vary the shape of the radial sections. The first digit represents the maximum camber, the second the position of the maximum camber, and the third and the forth the maximum thickness of the airfoil. In favour of lower computational efforts and faster convergence of the optimization the number of dimensioning parameters is kept low. These parameters describe the blade at three locations: the hub, the mid and the tip of the blade. Between those three radial positions, a linear interpolation is used to calculate the aerodynamic coefficients at every section.

## 4.3 Optimization Setup

The aim of the optimization is to find a rotor design which both satisfies the design condition and maximizes the annual energy yield. The optimization approach is illustrated in Fig. 4.4. CMA-ES uses the free dimensioning parameters $x_i$ to minimize the cost function $K$. CMA-ES is completely detached from the calculation scheme of XFoil and XRotor. If a rotor design delivers "false" for the constraints and the design condition, the cost function $K$ is negative and therefore closer to the intended minimum. The present section is focused on the input of XRotor,

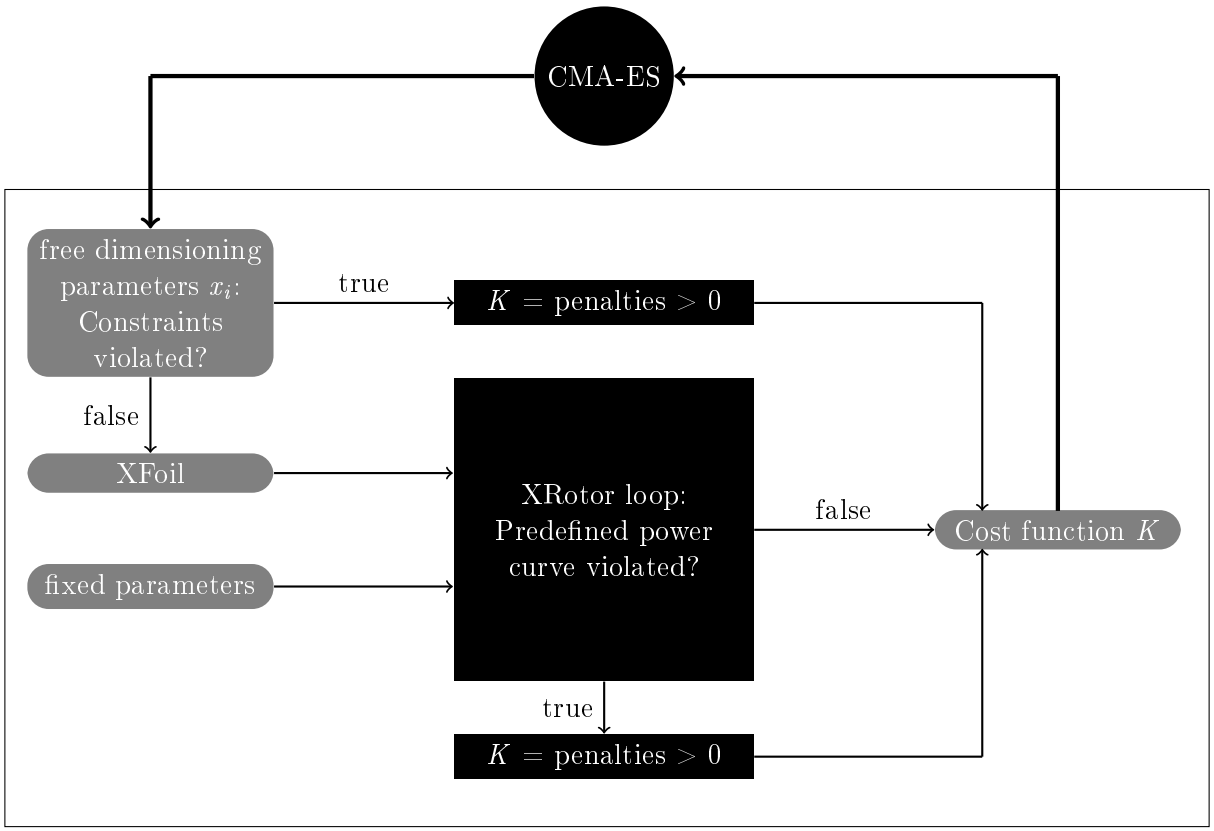


Figure 4.4: Optimization setup with the genetic algorithm CMA-ES in the black dot, the free dimensioning parameters $x_i$, the XFoil claculation and the fixed parametrs as input for the XRotor calculation loop in the center, the penalties if the design condition or the constraints get violated and the final cost function $K$ as input for CMA-ES.

the handling of the cost function via penalties, the design condition, and the cost function itself.

### 4.3.1 Input

As shown in the previous Sec. 4.2, the parametrization of the rotor is defined by 18 dimensioning parameters. Additional to those 18 dimensioning parameters, two further parameters are set as fixed values:

- $R_{tip}$ is limited by the wing span, the design structure, and the number of rotors used on the drag power kite. Increasing tip radius has a large positive influence on the rotor efficiency, which is why $R_{tip}$ should always be as high as possible.

- $R_{hub}$ is calculated by centrifugal loads acting on the rotor blade, and defines the area where the aerodynamic calculation of the rotor blade starts.

### Constraints and penalties

Constraints are implemented by upper $\bar{x}_i$ and lower $\underline{x}_i$ bounds of the free dimensioning parameters $x_i$. Violated constraints are handled by penalties $\delta_{I,i}$ for each dimensioning parameter $x_i$. Whenever CMA-ES changes the set of the free dimensioning parameters to start a new rotor calculation, the algorithm first verifies whether the selected parameters are inside the given bounds or not. For every $x_i < \underline{x}_i$ or $x_i > \bar{x}_i$ penalties $\delta_{I,i}$ are calculated as follows:

$$\delta_{I,i} = \begin{cases} (\bar{x}_i - x_i)^2 & \text{for} \quad x_i > \bar{x}_i \\ (\underline{x}_i - x_i)^2 & \text{for} \quad x_i < \underline{x}_i \end{cases}. \tag{4.9}$$

The initial value of the cost function is $K = 0$, redefined whenever CMA-ES varies the dimensioning parameters. After verifying the constraints, the cost function is given by

$$K = \sum_i \delta_{I,i}. \tag{4.10}$$

If one or more constraints are violated, the value of the cost function gets $K > 0$ and the XRotor calculation is skipped to directly communicate the positive value of the cost function with CMA-ES (Fig. 4.4) and hence avoid invalid values in the next iterations step by step. If all dimensioning parameters are verified and the resulting cost function is zero, XFoil supplies the drag and lift curves for the selected airfoils.

### XFoil

The free dimensioning parameters $x_i$ for $i = 10 - 18$ are defined in Sec. 4.2 as 4 digit NACA airfoils at the hub, in the mid and at the tip of the blade. As mentioned in Sec. 3.2, XRotor uses a linear $C_l - \alpha$ and a quadratic $C_d - C_l$ curve to calculate the airfoil coefficients, depending on the Reynolds number $Re$, the Mach number $Ma$, and the angle of attack $\alpha$. A MatLab code connected to XFoil is used to approximate the curves. This code is introduced in this section.

As a first step, the lift polar is computed and visualized in Fig. 4.5 for a symmetric and a cambered NACA airfoil. The dashed blue line is the lift polar $C_{l,XF}(\alpha)$ computed by XFoil. The

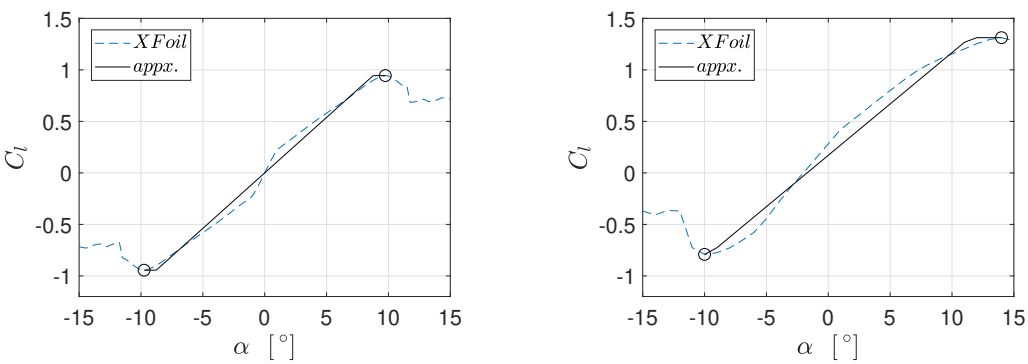


(a) NACA0010 (b) NACA2412

Figure 4.5: Lift polar diagrams for NACA 4 digit airfoils computed by XFoil with the resulting XRotor approximation. In Fig. 4.5a the lift coefficient $C_l$ of a symmetric NACA0010 airfoil is plotted over the angle of attack $\alpha$. In Fig. 4.5b the lift coefficient $C_l$ for a cambered NACA2412 is plotted over the angle of attack $\alpha$.

values for $C_{l,max}$ and $C_{l,min}$ are extracted and marked by a circle. In the next step, the XFoil lift polar is limited to the area between $C_{l,min}$ and $C_{l,max}$. Therefore, the linear fitting for XRotor is given by (black line in Fig. 4.5)

$$C_{l,XRfit}(\alpha) = c_{1,lin} + c_{2,lin}\alpha \quad \text{with} \quad \mathbb{D} = \{\, \alpha \in \mathbb{R} \mid \alpha_{C_{l,min}} < \alpha < \alpha_{C_{l,max}} \}. \tag{4.11}$$

Once the constants $c_{1,lin}$ and $c_{2,lin}$ are known, the code continues with the calculation of the XFoil drag polar shown in Fig. 4.6. As well as for the lift polar, the values for $C_{l,max}$ and $C_{l,min}$

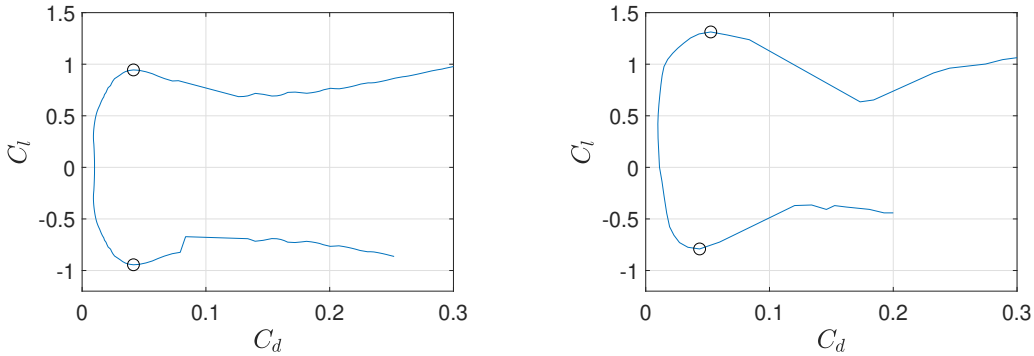


(a) NACA0010 (b) NACA2412

Figure 4.6: Drag polar diagrams for NACA 4 digit airfoils computed by XFoil. In Fig. 4.6a the lift coefficient $C_l$ of a symmetric NACA0010 airfoil is plotted over the drag coefficient $C_d$. In Fig. 4.6b the lift coefficient $C_l$ for a cambered NACA2412 is plotted over the drag coefficient $C_d$.

are marked by a circle. A simple quadratic fitting given by

$$\begin{aligned} C_{d,XRfit}(\alpha) &= c_{1,quad} + c_{2,quad}(c_{3,quad} - C_{l,XF}(\alpha))^2 \quad \text{with} \\ \mathbb{D} &= \{\, \alpha \in \mathbb{R} \mid \alpha_{C_{l,min}} < \alpha < \alpha_{C_{l,max}} \} \end{aligned} \tag{4.12}$$

is possible, but the approximation accuracy is crude. The accuracy can be increased by using the lift-to-drag ratio $E$ to approximate the drag polar. The lift-to-drag ratio is defined by

$$E = \frac{C_l}{C_d} = \frac{C_{l,XF}}{C_{d,XF}} \tag{4.13}$$

and shown in Fig. 4.7. A high lift-to-drag ratio is the primary objective in airfoil design for classical aircrafts, wind turbines, and propellers. The main approach to increase the lift-to-drag ratio lays in the use of cambered airfoils as seen in Fig. 4.7. To increase the accuracy of the drag

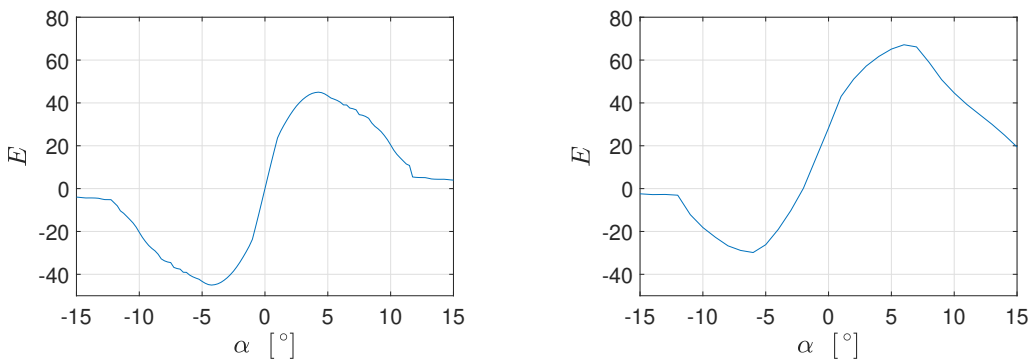


(a) NACA0010 (b) NACA2412

Figure 4.7: Lift-to-drag ratio $E$ for NACA 4 digit airfoils computed by XFoil. In Fig. 4.7a the lift-to-drag ratio $E$ of a symmetric NACA0010 airfoil is plotted over the angle of attack $\alpha$. In Fig. 4.7b the lift-to-drag ratio $E$ for a cambered NACA2412 is plotted over the angle of attack $\alpha$.

polar fitting, instead of the $C_{l,XF}(\alpha)$ polar from XFoil, the fitted polar $C_{l,XRfit}(\alpha)$ of Eq. 4.11

is inserted in Eq. 4.12 and divided by 4.11 in reverse. The equation for fitting the lift-to-drag ratio supplied by XFoil (Eq. 4.13, Fig. 4.7) is therefore given by

$$\begin{aligned} E_{XRfit}(\alpha) &= \frac{C_{l,XRfit}(\alpha)}{C_{d,XRfit}\left(C_{l,XRfit}(\alpha)\right)} \quad \text{with} \quad \mathbb{D} = \{\alpha \in \mathbb{R} \mid \alpha_{C_{l,min}} < \alpha < \alpha_{C_{l,max}}\} \\ &= \frac{c_{1,lin} + c_{2,lin}\alpha}{c_{1,quad} + c_{2,quad}(c_{3,quad} - (c_{1,lin} + c_{2,lin}\alpha))^2}. \end{aligned} \tag{4.14}$$

The approximated lift-to-drag ratio $E_{XRfit}(\alpha)$ is sketched in black in Fig. 4.8, the dashed blue line represents the original lift-to-drag ratio supplied by XFoil. The quadratic drag polar for

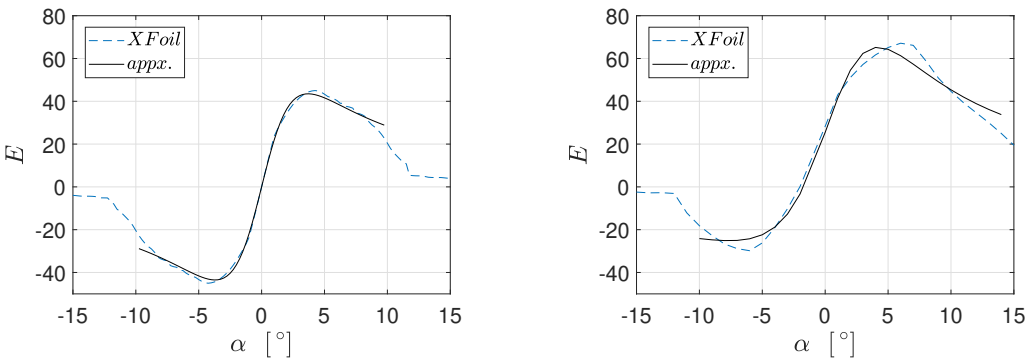


(a) NACA0010 (b) NACA2412

Figure 4.8: Lift-to-drag ratio $E$ for NACA 4 digit airfoils computed by XFoil and the appx. lift-to-drag ratio $E_{XRfit}$. In Fig. 4.8a the lift-to-drag ratio $E$ of a symmetric NACA0010 airfoil is plotted over the angle of attack $\alpha$. In Fig. 4.8b the lift-to-drag ratio $E$ for a cambered NACA2412 is plotted over the angle of attack $\alpha$.

XRotor is now given by the calculated constants by means of

$$C_{d,XRfit}(\alpha) = c_{1,quad} + c_{2,quad}(c_{3,quad} - (c_{1,lin} + c_{2,lin}\alpha))^2 \tag{4.15}$$

and shown in Fig. 4.9. The constants $c_{1-2,lin}$ and $c_{1-3,quad}$ are linearly interpolated for each

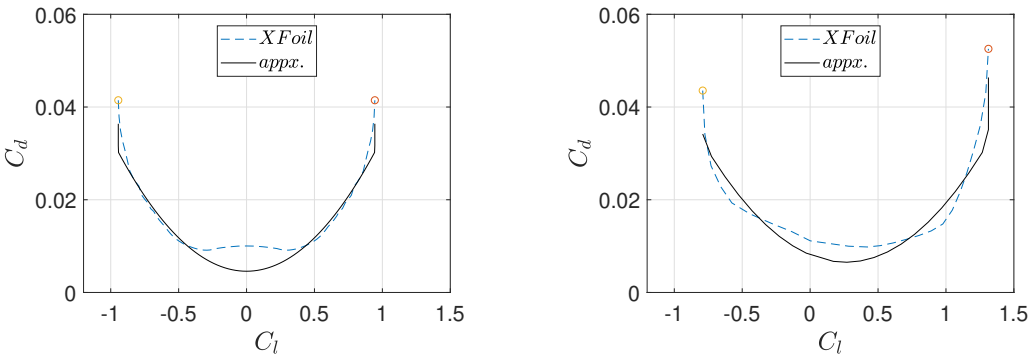


(a) NACA0010 (b) NACA2412

Figure 4.9: Drag polar diagrams for NACA 4 digit airfoils computed by XFoil and the appx. drag polar $C_{d,XRfit}$. In Fig. 4.9a the drag coefficient $C_d$ of a symmetric NACA0010 airfoil is plotted over the lift coefficient $C_l$. In Fig. 4.9b the drag coefficient $C_d$ for a cambered NACA2412 is plotted over the lift coefficient $C_l$.

section along the radius, and transmitted to XRotor together with the Reynolds and Mach number for the individual scaling. All calculations in XFoil are performed in viscous mode,

which means that compressibility effects are considered by the Karman-Tsien compressibility correction [22].

### 4.3.2 Verification of the Design Condition

The thrust of the rotor at different inflow velocities is the predefined design condition to guarantee that the optimal power curve is achieved (shown in Fig. 4.2). The thrust supplied by a rotor is limited by various factors, and a simplified sketch is shown in Fig. 4.10. The main factor is the

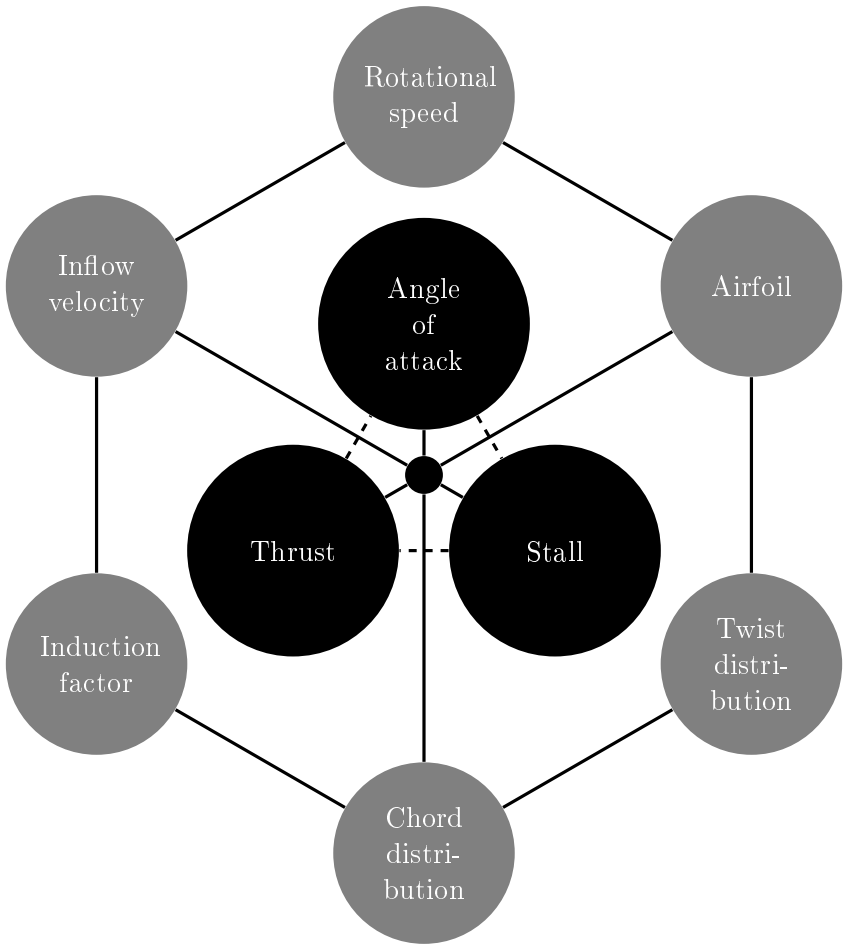


Figure 4.10: Thrust, Stall, Angle of attack in the center and connected by a triangle and surrounded by the influencing parameters in the grey dots.

angle of attack $\alpha$ for each section along the radius, which is influenced by the remaining factors depicted in the gray circles on the other hand.

Depending on the Reynolds number and the Mach number, a given airfoil stalls at a certain angle of attack. As illustrated in Fig. 4.5, the stall occurs when $C_{l,max}$ is reached. When a airfoil starts to stall, it looses lift and therefore the rotor looses thrust.

Fig. 4.10 also contains the free dimensioning parameters, which are represented by the chord distribution, the twist distribution, and the airfoils. The triangle consisting of the angle of attack, the supplied thrust, and stall can be directly influenced by CMA-ES by changing the free dimensioning parameters. The rotational speed is a further degree of freedom to influence the triangle. In contrast to the free dimensioning parameters, the rotational speed is not regulated by CMA-ES. The defined range of the rotational speed is limited by the tip Mach number $Ma < 0.5$. The range of the rotational speed allows for the calculation of different thrust values at a constant inflow velocity, which is a main requirement to verify the design condition and to set up a rotor

control for crosswind flight. The range of the inflow velocity is predefined and equal to the range of the true airspeed $v_a$. The induction factor (labeled as $a_{ind}$) is a result of the supplied thrust and has a direct influence on the angle of attack but is not available to regulate the angle of attack.

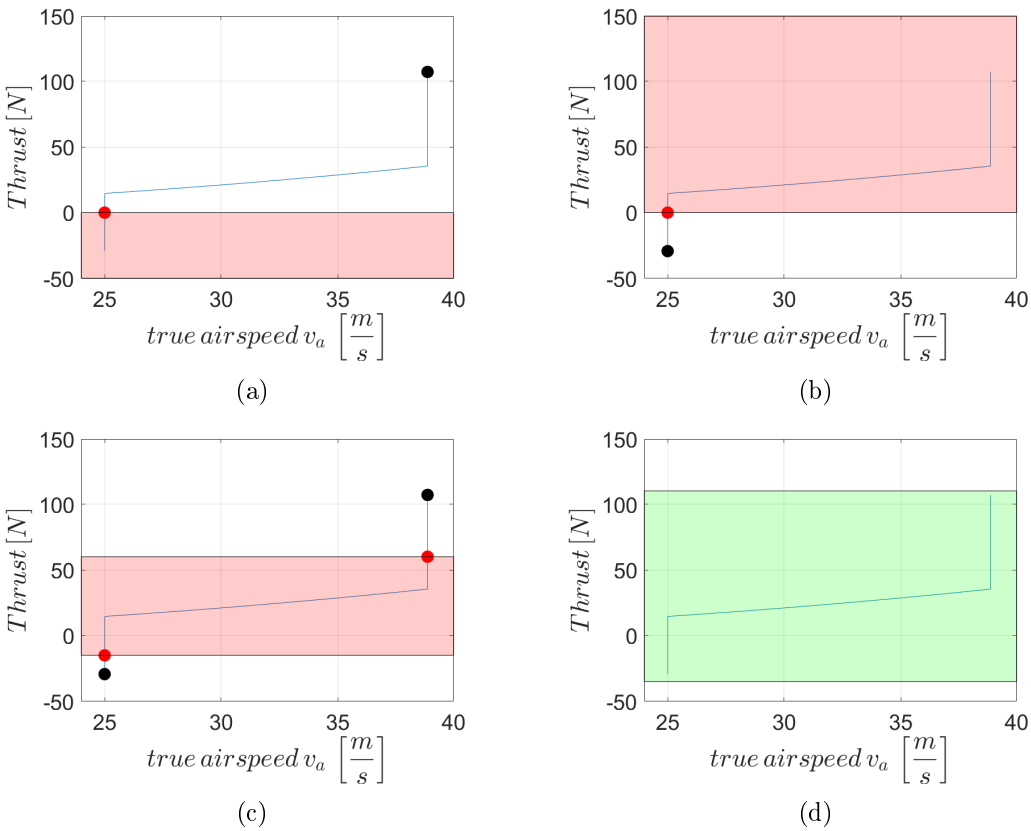


Figure 4.11: Thrust capacity of a given rotor design calculated by the XRotor loop compared to the design condition. Fig. 4.11a, 4.11b and 4.11c show the case when the design condition is violated. Fig. 4.11d shows the case when the design condition is fulfilled.

In case the rotor design of the current iteration of CMA-ES does not violate the constraints (Sec. 4.3.1), and the cost-funstion is $K = 0$, the optimization setup continues with the XRotor loop (Fig. 4.4). It is called a loop because XRotor is run several times to calculate a set of thrust values for each inflow velocity by changing the rotational speed within a given range. Possible results of the XRotor loop are shown in a simplified illustration in Fig. 4.11. The blue line represents the thrust predefined by the power curve. The red zone illustrates the thrust values the rotor can supply with the current rotor design without reaching stall. To keep the Fig. simple and focus on the verification of the design condition, the diagram is shown two-dimensional. The full resolution would be a three-dimensional diagram with the rotational speed on the third axis.

First, we take a look at on Fig. 4.11a. The rotor thrust covers only negative thrust values of the design condition, which means that the current rotor design only works in motor mode. The complete generator mode is not covered by the rotor thrust values because multiple airfoil sections along the blade achieve the angle of attack where stall occurs and the absolute thrust values decreases. The design condition is violated and equal to Eq. 4.9 and 4.10 the cost function gets $K > 0$ (Fig. 4.4). To calculate the penalty $\delta_{II}$, the black dot is declared as the maximum thrust of the design condition $T_{max,DC}$, and the red dot as the maximum thrust supplied by XRotor $T_{max,XR}$. The same declaration is made for the negative values in Fig. 4.11b. Like this,

the penalty $\delta_{max}$ can be calculated by

$$\delta_{II,max} = (T_{max,DC} - T_{max,XR})^2 \quad \text{for} \quad T_{max,DC} > T_{max,XR}, \tag{4.16}$$

and

$$\delta_{II,min} = (T_{min,DC} - T_{min,XR})^2 \quad \text{for} \quad T_{min,DC} < T_{min,XR}. \tag{4.17}$$

In Fig. 4.11c, another possible case is shown. The rotor thrust neither covers the complete motor mode nor the complete generator mode. Both equations 4.16 and 4.17 are applied to calculate the penalties. The final cost function is given by

$$K = \delta_{II,max} + \delta_{II,min}. \tag{4.18}$$

The last Fig. 4.11d is covered by a green zone, which means that the rotor thrust fulfills the design condition and the cost function passes with $K = 0$.

### 3D-Rotor-Map

The constraints and the design condition for the current rotor design are fulfilled, and the XRotor loop has been calculated. As mentioned before, the diagrams in Fig. 4.11 are limited to a two-dimensional view to focus on the calculation of the penalties. To continue with the design procedure, the rotor performance is plotted in a three-dimensional space with the coordinate system shown in Fig. 4.12. The rotational speed $rpm$ is plotted along the x-axis, the true

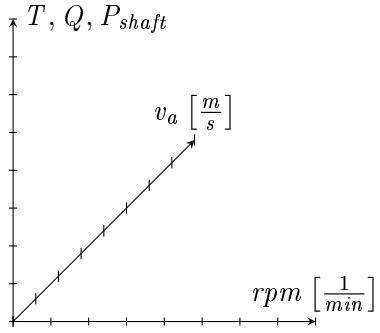


Figure 4.12: 3D coordinate system for the rotor performance data. Along the x-axis the rotational speed $rpm$, along the y-axis the true airspeed $v_a$, and along the z-axis the performance data consisting of the thrust $T$, the torque $Q$, and the shaft power $P_{shaft}$.

airspeed $v_a$ along the y-axis, and the values for the rotor performance along the z-axis. The rotor performance data consists of the thrust $T$, the torque acting on the shaft $Q$, and the shaft power $P_{shaft}$. The complete rotor performance is supplied by XRotor. As shown in Sec. 4.1, for every wind speed $v_w$ a true airspeed $v_a$ is given with a matching thrust value $T_{DC}$ from the design condition. This can be expressed in the form of

$$T_{DC} = f(v_a). \tag{4.19}$$

This is independent from the rotational speed in the third axis. The equation system of the set of thrust values supplied by the XRotor loop with the current rotor design $T_{XR}$ is given in the form of

$$T_{XR} = f(v_a, rpm). \tag{4.20}$$

A exemplary three-dimensional plot of $T_{XR}$ and $T_{DC}$ is shown in Fig. 4.13. $T_DC$ is visualized as a black surface, which is independent from the rotational speed. $T_{XR,set}$ is visualized by a colored surface and depends on the rotational speed and the true airspeed. In retrospect, the design condition is approved if the black surface is completely surrounded by the the colored

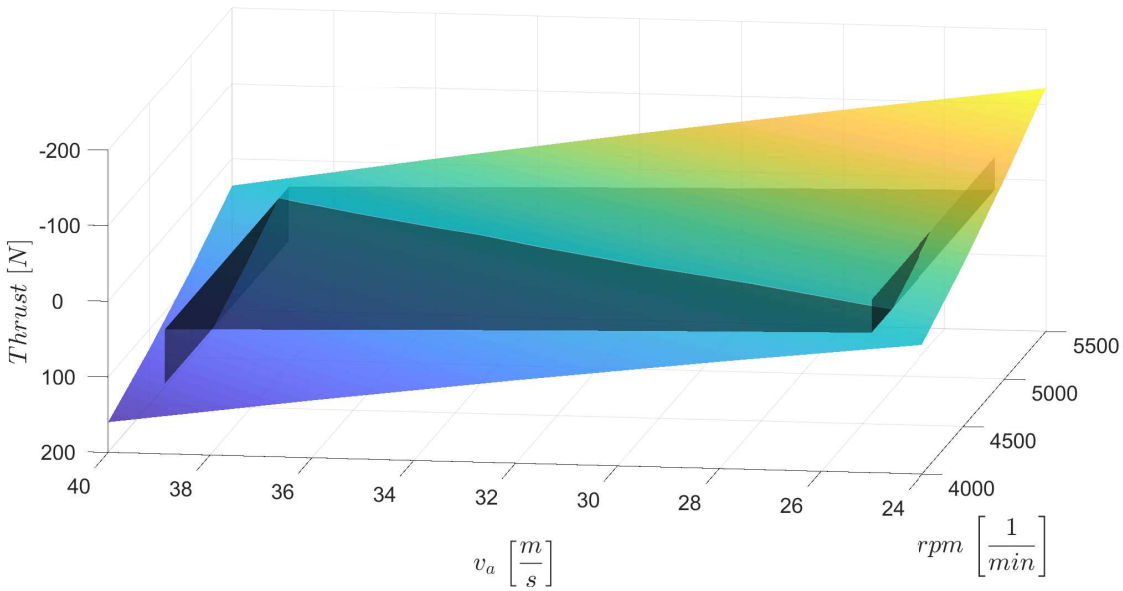


Figure 4.13: Exemplary XRotor loop for the thrust values $T_{XR}$ plotted with the design condition $T_{DC}$. Along the x-axis the rotational speed $rpm$, along the y-axis the true airspeed $v_a$, and the thrust $T$ along the z-axis.

surface. The next step is to figure out at which rotational speeds the current rotor design supplies exactly the thrust values to satisfy the design condition, which is simply the intersection of the black and the colored surface. To find the matching rotational speeds, a three-dimensional linear interpolation is performed. Based on the newly generated rotational speeds and the predefined true airspeeds, the three-dimensional linear interpolation can be repeated in the reverse way to extract the matching torque $Q$ and shaft power $P_{shaft}$ out of the rotor performance data.

### 4.3.3 Cost Function

With the obtained shaft power $P_{shaft}$ the annual energy yield $E_{el,yr}$ can be calculated (Eq. 3.24). The main goal of the optimization procedure is to maximize the energy output of the drag power kite. Therefore, the cost function is set to be the negative value of the annual energy yield by

$$K = -E_{el,yr} = -\frac{8,760\,h}{1\,yr} \int_0^\infty p(v_w) P_{shaft+}(v_w)\, dv_w \tag{4.21}$$

The efficiency of a rotor in generator mode is defined by Eq. 3.23 and therefore the shaft power can be expressed by

$$P_{shaft} = \eta_{gen}\, T v_a. \tag{4.22}$$

The thrust $T$ and and true airspeed $v_a$ are predefined, and therefore the cost function can be interpreted as the rotor efficiency multiplied with the probability of the certain wind speed and integrated over the range of wind speeds:

$$K \propto -\int_0^\infty p(v_w) \eta_{gen}(v_w)\, dv_w. \tag{4.23}$$

## 4.4 Validation of the Optimized Rotor

The theory of XRotor is based on the lifting line theory. To validate the calculations made with the lifting line theory, the BEMT has been implemented in MatLab. A simplified introduction

in the procedure of the BEMT is shown in Fig. 4.14. To increase the accuracy of the BEMT, XFoil is included in the calculation scheme. The BEMT splits the blade in radial sections and iteratively calculates the induction factors for every section. As the induction factors have a big influence on the angle of attack and the Reynolds and Mach number, XFoil is called for every iteration to supply the accurate aerodynamic coefficients $C_l$ and $C_d$. Therefore, the Reynolds and Mach scaling as well as the stall prediction for the NACA airfoils are calculated by the established panel-method of XFoil. All calculations of XFoil are performed in viscous mode, and the Prandtl tip loss model is embedded in the BEMT. The viscous mode includes the Karman-Tsien compressibility correction [22].

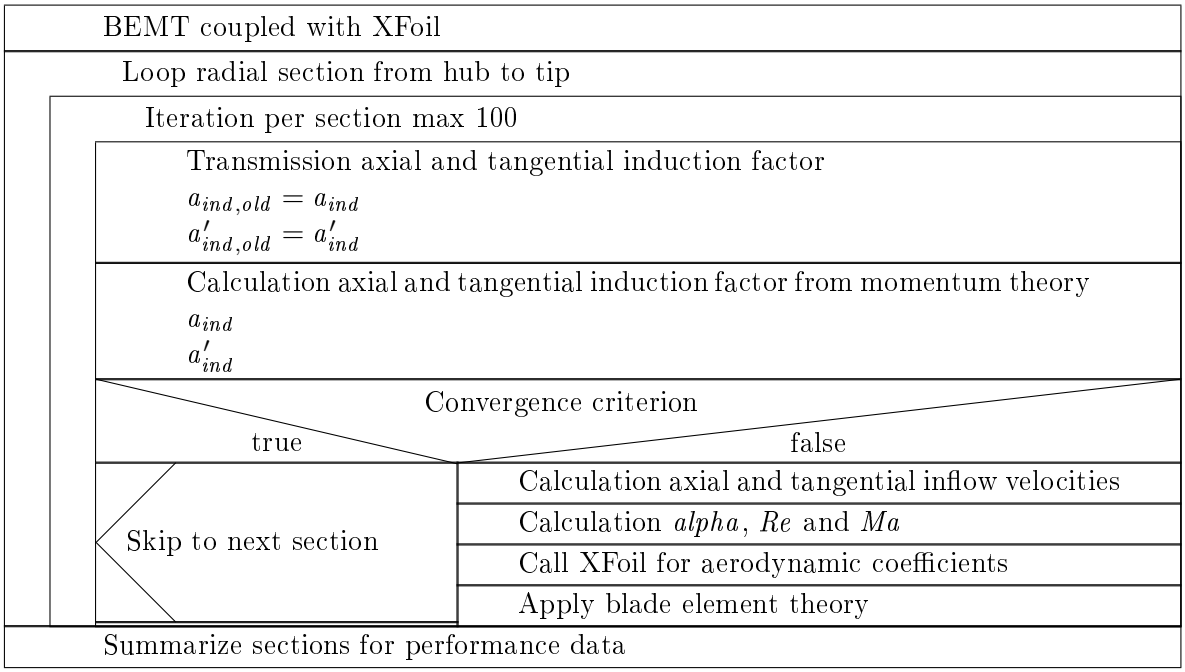


Figure 4.14: BEMT coupled with XFoil. Shown are two nested loops. Every section from hub to tip is iterative calculated by the momentum theory and the blade element theory with a maximum iteration number of 100. For every iteration XFoil is called.

Chapter 5

# Results

The rotor optimization of the previous chapter is applied for a drag power kite design performed by Bauer [4, Chapter 5.2.5]. The extracted data out of Bauer's kite design, is listed in the first section and forms the basis for the optimization. This section presents the optimized rotor design. Followed by the calculation of the rotor performance data by XRotor and the BEMT to validate the results of the used lifting line theory in the optimization procedure. In the end, a detailed aerodynamic analysis is performed to estimate the accuracy of the results.

## 5.1 Predefined Rotor Parameter

In table 5.1 the general rotor setup is listed. The curves for the true airspeed, the wind speed, the

| Predefined design input | | |
|---|---|---|
| Description | Symbol | Values |
| True airspeed $\left[\frac{m}{s}\right]$ | $v_a$ | 25 - 39 |
| Wind speed $\left[\frac{m}{s}\right]$ | $v_w$ | 0 - 25 |
| Probability wind speed $\left[\frac{m}{s}\right]$ | $p(v_w)$ | Fig. 5.6 |
| Thrust $[N]$ | $T$ | -35 - 107 |
| Aerodynamic power $[kW]$ | $P_a$ | -0.9 - 4.2 |
| Number of blades | $N_b$ | 3 - 7 |
| Rotor radius $[m]$ | $R_{tip}$ | 0.32 |
| Max. tip Mach number | $Ma_{tip}$ | $<$0.5 |

Table 5.1: Predefined design inputs.

aerodynamic power, and the thrust are shown in Fig. 4.1 and 4.2. The used Weibull probability distribution for a certain wind speed is shown in Fig. 5.1. As the probability distribution is

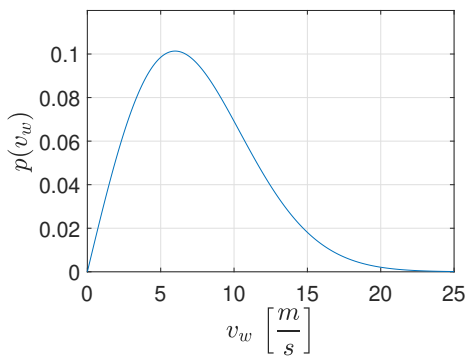


Figure 5.1: Weibull probability distribution for certain wind speeds. The probability $p(v_w)$ is plotted over the wind speed $v_w$.

implemented in the cost function, the impact of the distribution on the optimized rotor design is significant. The wind conditions are driven by the global circulation and heavily depend on the location where the kite operates. Therefore, it is highly valuable to individualize the rotor design for the respective location by adapting the implemented probability distribution to the local wind conditions.

Fig. 5.2 shows the rotor efficiency $\eta$ plotted over the wind speed $v_w$ and rated over the probability distribution $p(v_w)$ for a optimized three-blade, five-bladed and seven-bladed rotor. The deviations between the different blade number configurations are vanishingly low. The annual energy yield of the five-bladed rotor is slightly higher than the energy yield from the three- and seven-bladed rotor. Therfore, the five-bladed rotor is selected in the further presentation.

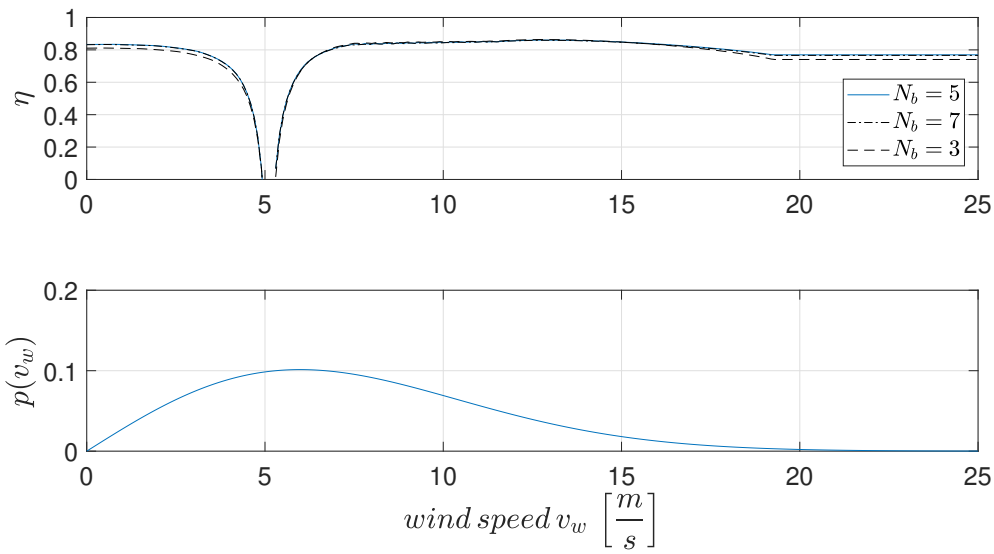


Figure 5.2: Comparison of a three-bladed, a five-bladed, and a seven-bladed rotor. The rotor efficiency $\eta$ is plotted over the wind speed $v_w$ and rated over the probability distribution $p(v_w)$.

The tip radius is given by the kite design and set to the maximum possible value. The tip Mach number is limited to $Ma < 0.5$ to keep the noise emissions of the rotor relatively low.

## 5.2 Optimized Rotor Design

The rotor design with the highest annual energy yield is shown in Fig. 5.3. According to Sec. 4.2, CMA-ES regulates the design by 18 free dimensioning parameters. Those parameters are used to define the chord and twist distribution (Fig. 5.3a and 5.3b ) and the blade shape at three radial positions (Fig. 5.3c).

The curve of the chord distributions shows a linear increase in the hub region, followed by a quadratic decrease to the tip. Between the linear and quadratic curves a small transition area is given. This means that the optimization of the chord distribution was not limited by a boundary of the free dimensioning parameter $x_1$, as the linear part does not directly pass over in the quadratic part. This can also be seen in table 5.2.

The parameters in the third column are the final optimized parameters. The neighbor columns two and four are filled with the corresponding boundaries of the free dimensioning parameters. According to Sec. 4.2 the first free dimensioning parameter $x_1$ defines the maximum possible chord value. The lower and upper bounds are set to $\underline{x}_1 = 0.1$ and $\bar{x}_1 = 0.3$, which means that the maximum chord value the blade can reach at any position along the radius is in the scope of 10 % and 30 % of $R_{tip}$. The optimized parameter has a value of $x_i = 0.21$ which results in a maximum chord of $c \approx 0.067\,m$ and can be seen in the chord distribution of Fig. 5.3a at

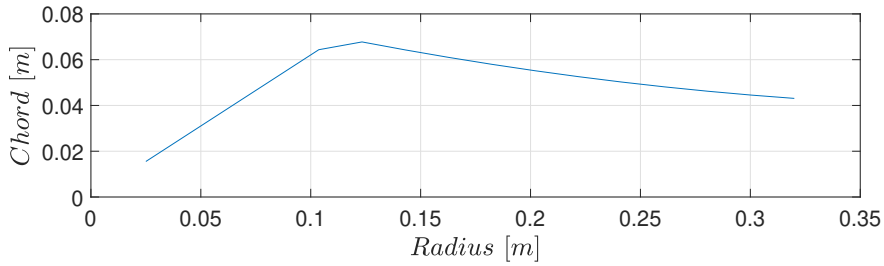


(a) Optimized chord distribution

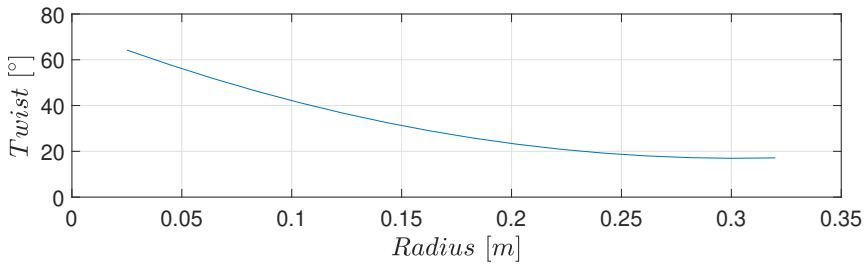


(b) Optimized twist distribution

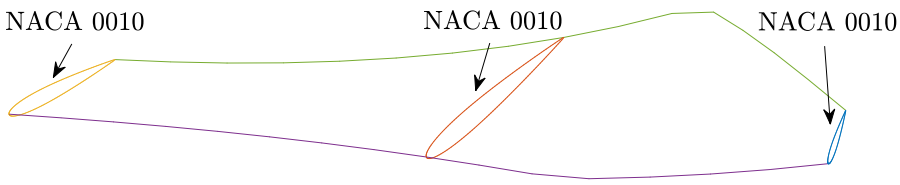


(c) Wire frame of the blade with the optimized airfoils

Figure 5.3: Optimized rotor design given by the chord, twist distribution, and airfoils. In Fig. 5.3a and 5.3b the chord and twist distribution are plotted over the radius. In Fig. 5.3c the wire frame of the optimized blade is given with NACA0010 airfoils at all three radial stations.

the radial position of $r \approx= 0.125\,m$. The next free dimensioning parameter $x_2$ defines the chord solidity in the hub region. The lower and upper bounds are set to $\underline{x}_2 = 0.25$ and $\bar{x}_2 = 0.75$, which means that chord solidity in the hub region the blades cover between 25 % and 75 % of the given area in the corresponding ring element. The gradient of the linear increase of the shape in the hub region can be directly calculated from $x_2 = 0.49$. The constraints of $x_1$ and $x_2$ avoid that the blades get in touch with each other in the hub region. The next values $x_3$ defines the maximum chord value between a radius of $\underline{x}_5 = 0.1\,m < r < \underline{x}_5 = 0.2\,m$ and is given as a percentage between 1 % and 90 % of the maximum chord value $x_1$. Therefore, the chord distribution is not able to increase in radial direction. The same procedure is applied for the last free dimensioning parameter of the chord distribution $x_4$. This approach is physically meaningful as the Reynolds number should be approximately constant along the radius. Furthermore, this approach supplies a faster convergence of the optimization. The optimized parameters of the chord distribution are all colored green, which means that the optimized chord distribution is not limited by a boundary.

The optimized twist distribution in Fig. 5.3b is approximated with a quadratic curve. The upper limit for the complete twist distribution is set to $\bar{x}_{i=6-8} = 70°$. The lower limit is set to $\underline{x}_{i=6-8} = 0.1°$. Negative values for the twist would not be affordable because the rotor would reduce its efficiency at all inflow velocities. The same approach as for the quadratic part of the

| Bounds of the free dimensioning parameters $x_i$ | | | |
|---|---|---|---|
| i | Lower bound $\underline{x}_i$ | Opt. parameter $x_i$ | Upper bound $\bar{x}_i$ |
| Chord | | | |
| 1 | 0.1 | 0.21 | 0.30 |
| 2 | 0.25 | 0.49 | 0.75 |
| 3 | 0.01 | 0.88 | 0.9 |
| 4 | 0.01 | 0.72 | 0.9 |
| 5 | 0.1 | 0.17 | 0.2 |
| Twist | | | |
| 6 | 0.1 | 64.25 | 70 |
| 7 | 0.1 | 32.23 | 70 |
| 8 | 0.1 | 17.14 | 70 |
| 9 | 0.1 | 0.14 | 0.2 |
| Airfoils | | | |
| 10 | 0 | 0 | 6 |
| 11 | 0 | 0 | 4 |
| 12 | 10 | 10 | 18 |
| 13 | 0 | 0 | 6 |
| 14 | 0 | 0 | 4 |
| 15 | 10 | 10 | 18 |
| 16 | 0 | 0 | 6 |
| 17 | 0 | 0 | 4 |
| 18 | 10 | 10 | 18 |

Table 5.2: Verification of the boundaries of the optimized parameters. First column are the index $i$, the second and the fourth are the lower $\underline{x}_i$ and upper bounds $\bar{x}_i$ of the free dimensioning parameters $x_i$. Green values indicate that the optimization was not limited by the bounds, red values indicate the opposite.

chord distribution is applied for the twist distribution. Consistent with the chord distribution, the optimized twist distribution is not limited by boundaries.

The optimized airfoils are shown in Fig. 5.3c. The optimization yield that symmetric airfoils NACA0010 are selected to reach the global minimum of the cost function and therefore to maximize the annual energy yield. In contrast to the optimized twist and chord distribution, the optimized airfoils are limited by its boundaries, as seen in table 5.2 by the red colored parameters. A symmetric airfoil has no camber and therefore the first two digits are zero. The optimization was free to increase the maximum camber up to 6% of the chord length at the variable camber position from $0 - 40\%$ of the chord length. The boundaries of the airfoil's thickness were set to be between $10 - 18\%$ of the chord length. Due to lack of solidity a lower thickness than 10% is not recommendable. The red colored values in table 5.2 indicate that the boundaries limit the optimization. The reasoning why the optimization prefers thin symmetric airfoils is discussed in a later section in detail.

The present section is closed by the CAD-Model of the five-bladed optimized rotor design in Fig. 5.4. The chord distribution is split by the 25%-line. This means that at every radial position 25% of the chord length are used to define the leading edge of the blade and the other 75% to define the trailing edge. Hence, the 25%-line points straight outward in radial direction.

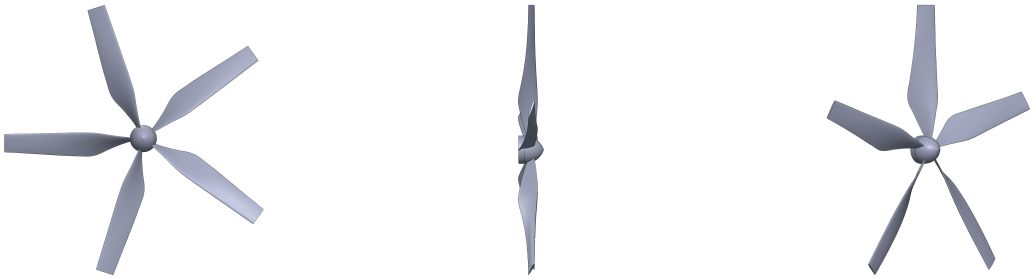

(a) Front view (b) Side view (c) Perspective view

Figure 5.4: CAD-Model of the optimized five-bladed rotor. In Fig. 5.4a in a front view, in Fig. 5.4b in a side view, and in Fig. 5.4c in a perspective view.

The annual energy yield of the optimized rotor is

$$E_{el,yr} = 31,800 \, \frac{kWh}{yr}.$$

All efficiencies of the powertrain components are included conformable to Bauer [4, Chapter 2.5].

## 5.3 Performance Data

The performance data is calculated and presented in the following by the thrust $T$ the shaft power $P_{shaft}$ and the torque $Q$. Those values depend on the optimized rotor design and can directly be calculated if the inflow velocities (= true airspeeds $v_a$) and the rotational speed $rpm$ are known. In our case, we only know the inflow velocities $v_a$, but we do not know the rotational speeds to exactly supply the predefined thrust values $T_{DC}$. Therefore, XRotor varies the rotational speed and calculates a set of thrust values $T_{XR}$ for each inflow velocity, called a XRotor loop. The result is a three-dimensional map as explained in Sec. 4.3.2.

The three-dimensional map with the thrust values $T_{XR}$ of the optimized rotor design is shown in Fig. 5.5. The rotational speed $rpm$ is plotted along the x-axis, the inflow velocity $v_a$ along the y-axis, and the rotor thrust along the z-axis. The black transparent surface is the design condition $T_{DC}$. Negative values indicate the motor mode, where energy is consumed with $P_{shaft} < 0$, and positive values indicate the generator mode with $P_{shaft} > 0$.

### 5.3.1 3D-Rotor-Map

Keeping the rotational speed constant, the thrust of the rotor increases with the inflow velocity $v_a$ approximately linear. The positive thrust is used as a additional drag force to brake the kite and harvest energy. The $T_{XR}$-$v_a$ relation can be attributed to the increasing angle of attack $\alpha$ with an increasing inflow velocity. The same behavior appears by keeping the inflow velocity $v_a$ constant and decreasing the rotational speed $rpm$. At low rotational speeds the rotor thrust map looks tattered. The stepped edge at low rotational speeds indicates that the rotor is starting to loose thrust in this area. The curve from high to low rotational speeds at a constant inflow velocity stagnates. This indicates that partial stages of the rotor blade are starting to stall. The optimization tries to get the intersection of the maximum needed rotor thrust $T_{DC,max}$ with the supplied rotor thrust $T_{XR}$ (marked by a red dot in Fig. 5.5) as close as possible to the stall region without entering the stall region.

To understand this behavior, a deeper look in the aerodynamics of an NACA0010 airfoil is necessary. In Fig. 4.5, the lift polar is plotted. The region where stall occurs is marked by a circle and located at $\alpha \approx 10°$ and $C_l \approx 1$. If all blade sections exemplary work above

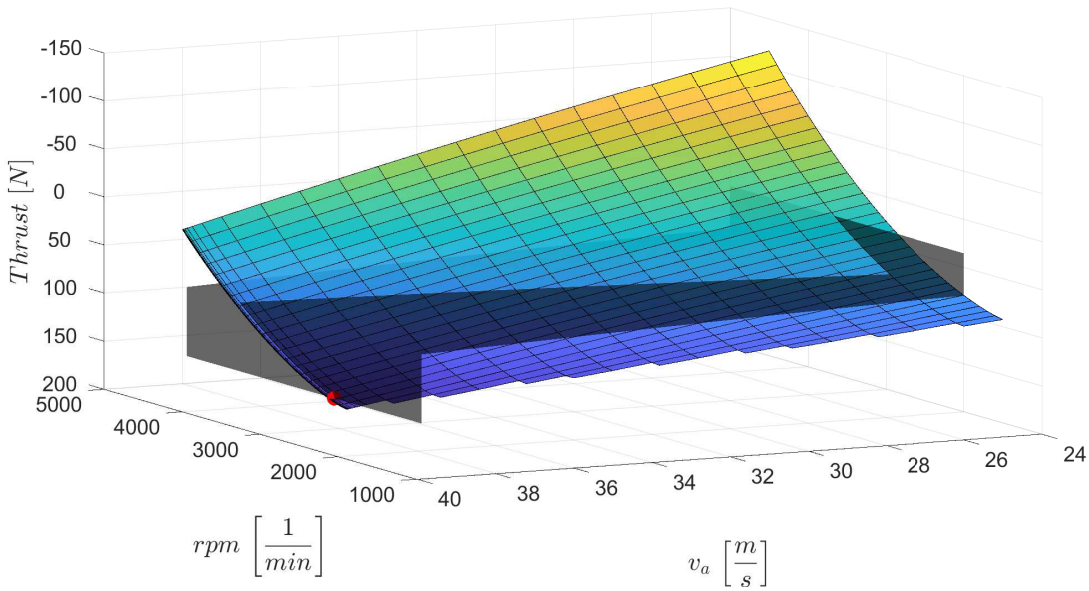


Figure 5.5: XRotor loop for the thrust values $T_{XR}$ of the designed rotor plotted with the design condition $T_{DC}$. Along the x-axis the rotational speed $rpm$, along the y-axis the inflow velocity $v_a$, and along the z-axis the thrust $T$.

the area with $\alpha > 10°$, the rotor would not produce thrust and work in stall completely. The region where the airfoil reaches the largest efficiency is between $3° < \alpha < 9°$ and therefore close to the stall region (Fig. 4.7a). In Fig. 5.6, the design condition $T_{DC}$ is plotted over the wind speed $v_w$ with the corresponding inflow velocity and rated over the Weibull distribution. At wind speeds of $v_w > 5\,\frac{m}{s}$ the generator mode starts, and the probability $p(v_w)$ for wind speeds between $5\,\frac{m}{s} < v_w < 12\,\frac{m}{s}$ is relatively high. Therefore, the main focus of CMA-ES is to optimize this region by keeping the angles of attack $\alpha$ in the previous mentioned area with the high efficiency. This is realized by CMA-ES by placing the intersection of the maximum needed rotor thrust $T_{DC,max}$ with the supplied rotor thrust $T_{XR}$ (marked by a red dot in Fig. 5.5) as close as possible to the stall region.

Once the 3D-map with the $T_{XR}$- and the $T_{DC}$-values is plotted, the intersection curve between the black and the colored surface is searched. The values that are left to describe the intersection curve are the rotational speeds $rpm_{rot}$, where the designed rotor supplies the thrust $T_{DC}$. To find the values for the matching rotational speeds, a three-dimensional linear interpolation with a stepsize of $v_{a,step} = 0.1\,\frac{m}{s}$ is used. Now, the final rotor thrust curve can be expressed by

$$T_{DC} = T_{rot} = f(v_{a,rot}, rpm_{rot}). \tag{5.1}$$

With the given values for $v_{a,rot}$ and $rpm_{rot}$, the three-dimensional linear interpolation can be used in reverse to find the matching values for the torque $Q_{rot}$ and the shaft power $P_{shaft,rot}$. This procedure is shown in Fig. 5.7 for the shaft power. Again, the rotational speed is plotted along the x-axis, the inflow velocity along the y-axis, and the shaft power along the z-axis. Negative values indicate the motor mode, where energy is consumed with $P_{shaft} < 0$, and positive values indicate the generator mode with $P_{shaft} > 0$. The behavior of the power map is connected to the behavior of the thrust map and can be explained in the same way as with an increasing thrust the power output increases as well.

The red intersection curve is the solution of the interpolation for the shaft power. The maximum power is reached where the red dot is located. In comparison to Fig. 5.5 the maximum shaft power is reached right before the stall region starts. The power map and the location of the red intersecting curve allows further power optimization. The extracted power could be further

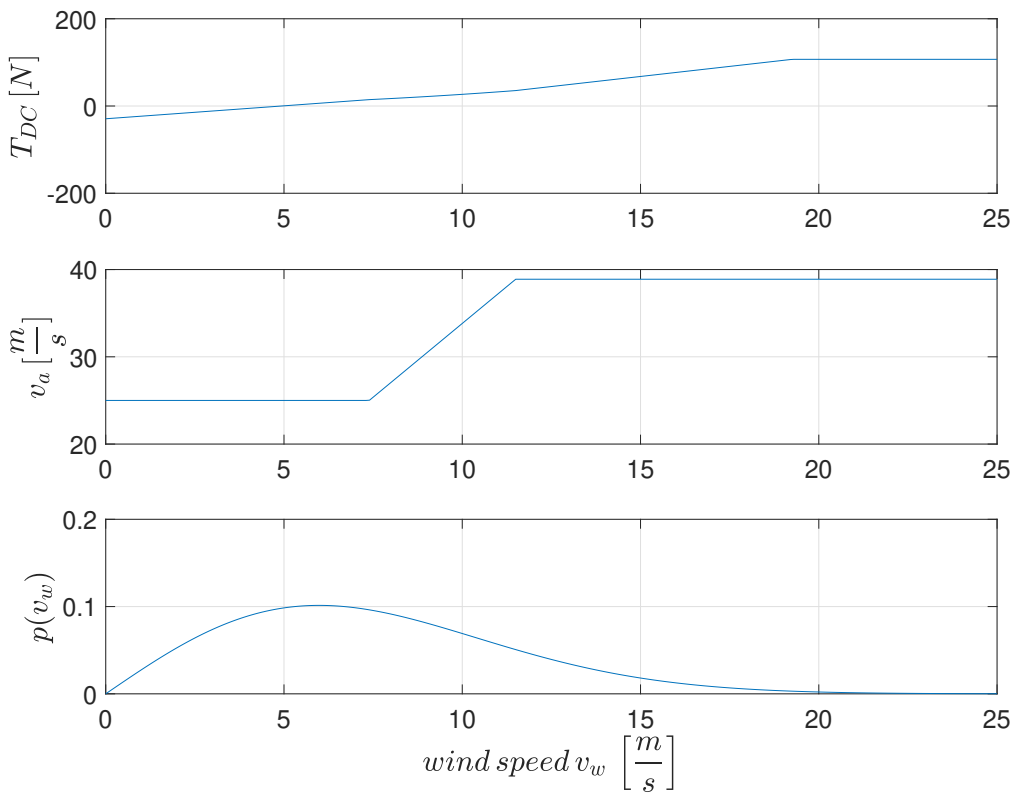


Figure 5.6: Design condition $T_{DC}$ plotted over the wind speed $v_w$, compared to the inflow velocity $v_a$, and rated over the probability distribution $p(v_w)$.

increased by allowing the rotor to enter the stall region at the point with the maximum power output. This would lead to a relocation of the intersection curve towards the power map valley in the main region between $25\,\frac{m}{s} < v_a < 39\,\frac{m}{s}$. At the bottom of the valley the highest power output is reached for given inflow velocities. This would also increase the cost function and can again be explained with Fig. 5.6. However, by entering the stall region, the rotor is no longer able to supply the required drag to fulfill the predefined power curve. Additional air-brakes could be a solution in this issue.

### 5.3.2 Power Output and Efficiency: XRotor vs BEMT

The BEMT is commonly used as a propeller design algorithm. In the present work the BEMT-code is coupled with XFoil to validate the results performed by the lifting line theory of XRotor. The coupling of the BEMT with XFoil is explained in Sec. 4.4. The comparison of the BEMT and XRotor is shown in Fig. 5.8. The shaft power $P_{shaft}$, the rotor thrust $T_{rot}$, the efficiency $\eta$, and the wind distribution $p(v_w)$ are plotted over the wind speed $v_w$.

The efficiency is calculated by Eq. 3.23 for motor- or generator mode. In transition from motor in generator mode the thrust of the rotor $T_{rot}$ has a zero-crossing. For the sake of simplicity, the relations are broken down to one airfoil section. The inflow velocity and the rotational speed confine an angle which corresponds to the local twist angle. The result is an angle of attack of $\alpha = 0$ and therefore only drag is produced without any lift. The transition point of the thrust is located at a wind speed of $v_w \approx 5\,\frac{m}{s}$. The transition point for the shaft power occurs at a slightly higher wind speed of $v_w \approx 5.5\,\frac{m}{s}$. As mentioned before, the angle of attack is $\alpha = 0$ and no lift is produced, but the rotor still consumes power to compensate the produced drag of the airfoil. As the shaft power and the thrust both have a zero-crossing, the efficiency gets $\eta = 0$ for wind

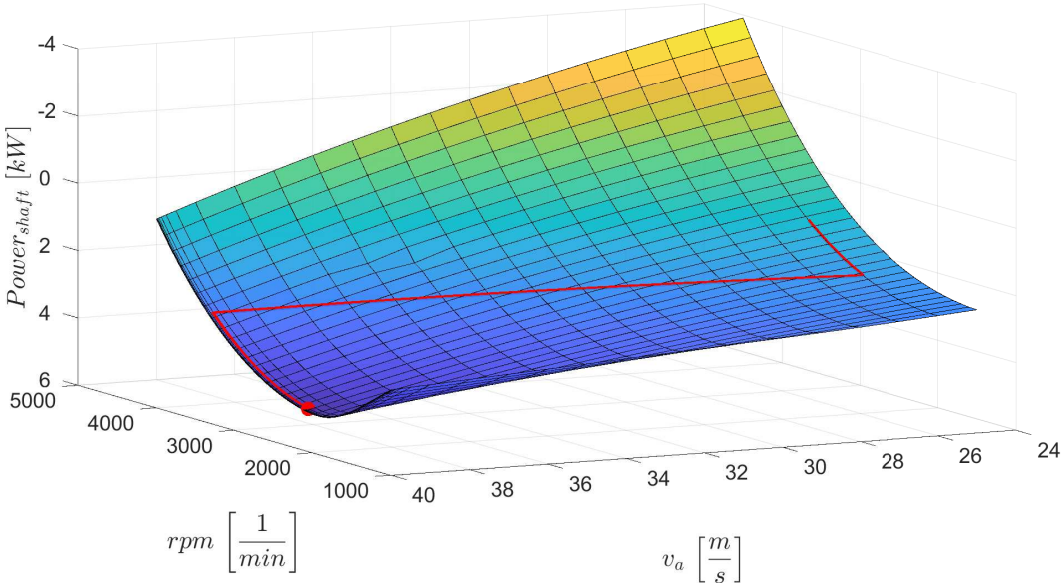


Figure 5.7: XRotor loop for the shaft power values $P_{shaft}$ of the designed rotor plotted with the intersection line from the given inflow velocities $v_a$ and the corresponding rotational speeds $rpm$. Along the x-axis the rotational speed $rpm$, along the y-axis the inflow velocity $v_a$, and along the z-axis the shaft Power $P_{shaft}$.

speeds between $5\,\frac{m}{s} < v_w < 5.5\,\frac{m}{s}$. The maximum efficiency calculated by XRotor is $\eta_{XR} = 86\,\%$ at a wind speed of $v_w \approx 12\,\frac{m}{s}$. The maximum efficiency calculated by the BEMT is $\eta_{XR} = 82.5\,\%$ at the same wind speed as for XRotor. The average efficiencies between $7\,\frac{m}{s} < v_w < 20\,\frac{m}{s}$ are $\eta_{XR} = 83.34\,\%$ and $\eta_{BEMT} = 79.6\,\%$, and therefore the average deviation for this wind speed parameter sets is 4.5 %. In total, the deviation between the efficiencies of the two calculations is rather low as seen in Fig. 5.8.

In motor mode the shaft power calculated by XRotor is higher than the shaft power calculated by the BEMT $P_{XR,shaft} > P_{BEMT,shaft}$. Therefore, the rotor calculated by the BEMT would consume more power in motor mode than the rotor calculated by XRotor. In generator mode the same behavior can be seen. The XRotor calculation supplies more generated power than the power generated by the BEMT. However, the deviations between the $P_{XR,shaft}$ and $P_{BEMT,shaft}$ are still rather low.

The same behavior can be seen for the thrust values. The XRotor calculation produces less thrust than the BEMT calculation. In other words, the XRotor calculations supplies a rotor with a fractional higher power output and a fractional lower thrust value, which in sum means that the rotor efficiency of the XRotor calculation is higher than the rotor efficiency of the BEMT calculation. In almost the entire figure the wind distribution is plotted to keep in mind that the optimization focuses on the wind speeds where the probability distribution reaches high values.

## 5.4 Detailed Analysis

In the following sections the rotor is analyzed by commonly used performance parameters in propeller and wind turbine design. The detailed analysis serves as a plausibility check of the optimized rotor design.

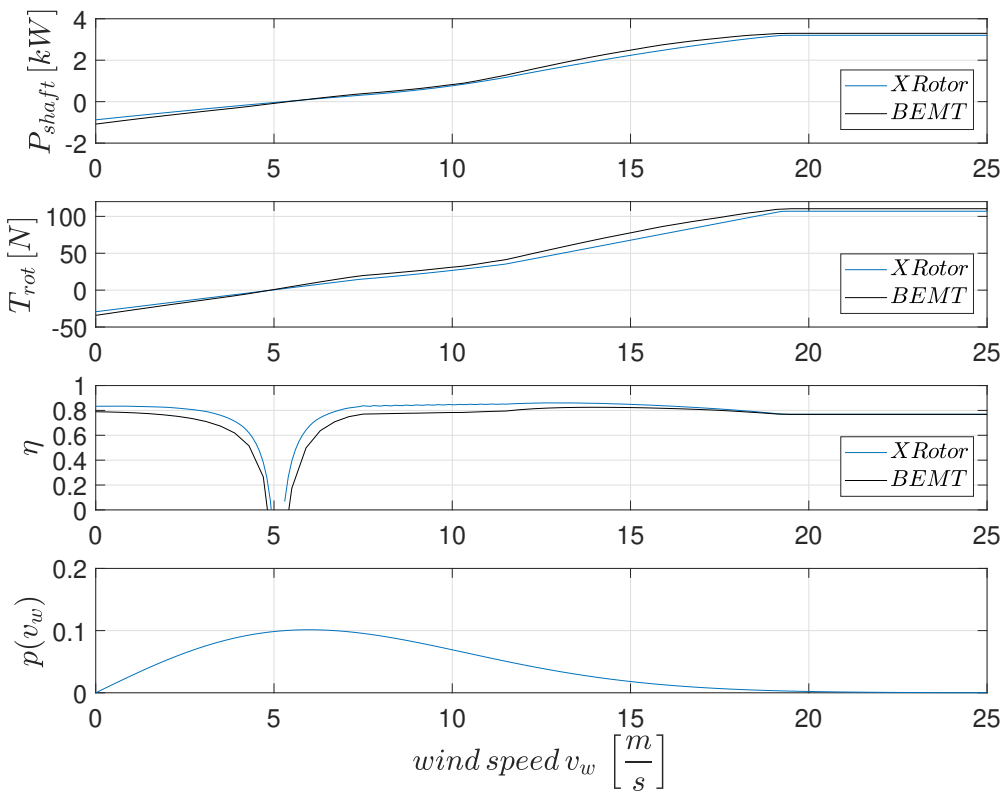


Figure 5.8: Comparison of the BEMT with the lifting line theory of XFoil based on the optimized rotor design. Compared with the shaft power $P_{shaft}$, the rotor thrust $T_{rot}$ and the efficiency $\eta$ plotted over the wind speed $v_w$ and rated over the probability distribution $p(v_w)$.

### 5.4.1 Rotor Torque with Reynolds and Mach Number

To complete the performance data (Sec. 5.3), the rotor torque $Q$ is plotted along the wind speed $v_w$. The shaft power of a rotor is given by the product of the rotational speed and the torque with

$$P_{shaft} = Q\, rpm\, \frac{2\,\pi}{60}. \tag{5.2}$$

Therefore, the rotor torque has the same zero-crossing point at $v_w \approx 5.5\,\frac{m}{s}$ as the shaft power, shown in Fig. 5.9. Aligned with Eq. 5.2, the rotational speed and the rotor torque are in equilibrium. The rotor design can be changed to get a rotor with higher rotational speeds and lower rotor torque but still the same shaft power. The result of the optimization shows that rotors with lower rotational speeds are more efficient. This can be explained by taking compressibility effects into account. With an increasing rotor speed, the tip velocity of the blade increases as well. The result of an increasing tip velocity is an increasing tip Mach number $Ma_{tip}$ shown in Fig. 5.10. For $Ma_{tip} > 0.3$ compressibility effects need to be considered. The compressebility effects have a negative impact on the rotor efficiency as energy is lost by compressing the air. In both calculations, XRotor and BEMT, a compressibility correction is considered.

On the other hand, the rotational speed also has a lower limit, the stall region (Sec. 5.3.1). Decreasing rotational speeds leads to higher angles of attack in generator mode. With an decreasing rotational speed the tangential inflow velocity seen by an airfoil section decreases as well and the angle of attack increases because the inflow velocity remains constant. Until a certain point, the higher angles of attack can be compensated by adjusting the twist distribution. However, this is only possible until the design condition in motor mode gets violated or the rotational speed is simple to low to avoid stall. The explanation of the appearance of stall at low rotational

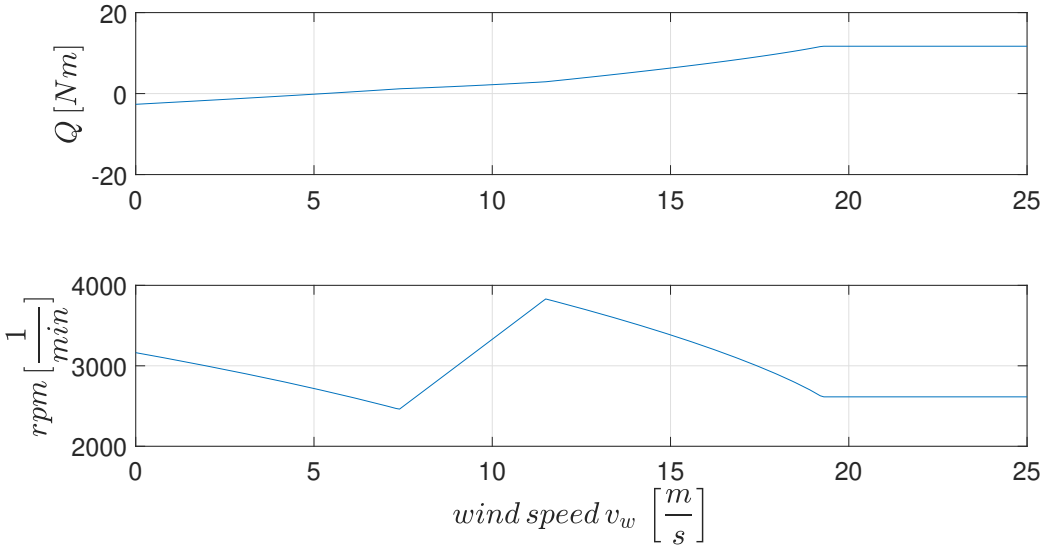


Figure 5.9: Rotor torque $Q$ and rotational speed $rpm$ plotted over the wind speed $v_w$.

speeds is the smaller amount of kinetic energy in a flow with lower speed relative to the airfoil. Thus, there is less energy saved to resist the rise in pressure along the airfoil, and therefore to resist stall.

Corresponding to the rotational speed, the rotor torque can not be increased limitless either. The onboard generators need to transmit the rotor torque and convert it into electrical energy. With an increasing rotor torque the mass and size of the generators increase as well. This leads to heavier drag power kites and results in a lower efficiency of the whole system. The minimum rotor torque is achieved in motor mode with $Q_{min} = -2.7\,Nm$, the maximum in generator mode with $Q_{max} = 11.7\,Nm$.

The tip Mach number $Ma_{tip}$ is plotted with the Reynolds number $Re$ (at 75 % of $R_{tip}$) and the probability distribution in Fig. 5.10, the maximum occurring tip Mach number is $Ma_{tip,max} = 0.38$ at a wind speed of $v_w = 11.6\,\frac{m}{s}$. The minimum occurring tip Mach number is $Ma_{tip,min} = 0.24$ at a wind speed of $v_w = 7.3\,\frac{m}{s}$. Hence, compressibility effects can be estimated as low.

The Reynolds number at 75 % of $R_{tip}$ varies between a maximum value of $Re_{max} = 3.5 \cdot 10^5$ and a minimum value of $Re_{min} = 2.3 \cdot 10^5$. The chord distribution keeps the Reynolds number approximately constant in radial direction. According to investigations of Yousefi [40], the lower critical Reynolds number for the transition from laminar to turbulent flow to start is $Re_{trans} = 1 \cdot 10^5$ for a NACA0010 airfoil. Based on those Reynolds numbers, the flow is assumed to be at least in transition from laminar to turbulent flow. The turbulence increases with the Reynolds number. A turbulent flow has the benefit of more kinetic energy saved in the flow, and therefore a higher resistance against stall. However, a turbulent flow also increases the drag of an airfoil, which has an influence on the efficiency as well.

### 5.4.2 Rotor Thrust Coefficient and Axial Induction Factor

The rotor thrust coefficient $C_T$ and the axial induction factor $a_{ind}$ are shown in Fig. 5.11. The thrust coefficient is defined in Eq. 4.1. Once the thrust coefficient is known, the axial induction factor can directly be calculated with the momentum theory by

$$C_T = 4a_{ind}(1 - a_{ind}). \tag{5.3}$$

The axial induction factor reaches in motor mode a minimum values of $a_{ind,min} = -0.06$ and in motor mode a maximum value of $a_{ind,max} = 0.1$. The corresponding values for the thrust

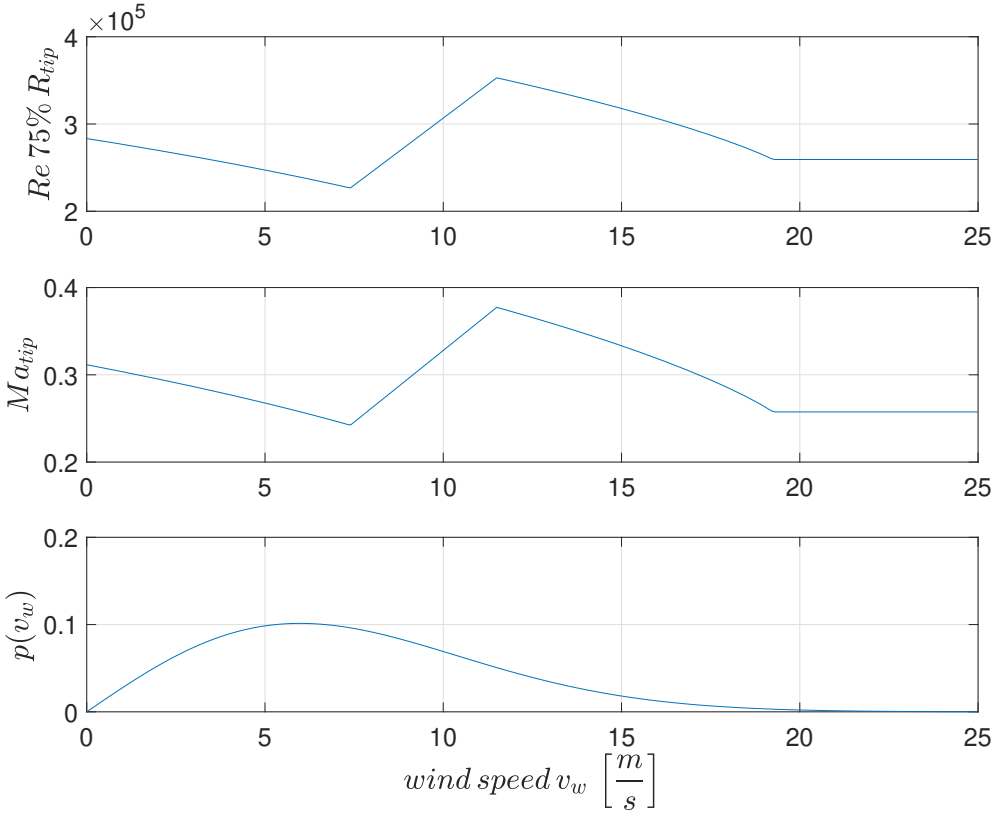


Figure 5.10: Reynolds number $Re$ at 75 % of the tip radius $R_{tip}$, and Mach number $Ma$ at the blade tip plotted over the wind speed $v_w$ and rated over the probability distribution $p(v_w)$.

coefficient by Eq. 5.3 are $C_{T,min} = -0.25$ and $C_{T,max} = 0.36$. In the classical propeller and wind turbine theory the axial induction factor and the thrust coefficient are used to describe the loading of a propeller. The loading can be interpreted as the force which acts on the propeller disk resulting from a pressure jump across the rotor disk. Lightly loaded rotors have a maximum axial induction factor of $a_{ind,light} = \pm 0.5$ and a maximum thrust coefficient of $C_{T,light} = \pm 1$. Rotors with higher values are treated as medium loaded propellers. The BEMT is not valid to calculate medium loaded propellers. In contrast, XRotor is also valid for medium loaded propellers but looses accuracy with an increasing loading.

A higher loading of a propeller leads to a lower efficiency. This can be explained by tip loss effects. A higher loading means a higher pressure jump across the rotor disk. At the tip of the blades the flow is not limited by a wall. The pressure gradient forces the flow at the tip to stream in radial direction and therefore avoid the rotor disk. The results are increasing tip vortices with an increasing loading. In the motion of the vortices energy is saved, which can not be extracted by the disk to increase the power output and therefore the efficiency.

The optimized rotor in the present work is designed as a lightly loaded highly efficient rotor. Even the maximum values for the axial induction factor and the thrust coefficient are in the scope of lightly loaded rotors. The main focus of the optimization points to the wind speeds, which occur with high probability. This area is given with $7\,\frac{m}{s} < v_w < 12\,\frac{m}{s}$. The values for the induction factor and the thrust coefficient are quite low in this area with $a_{ind} < 0.035$ and $C_T < 0.135$. Hence, blade tip loss effects are estimated to be rather low.

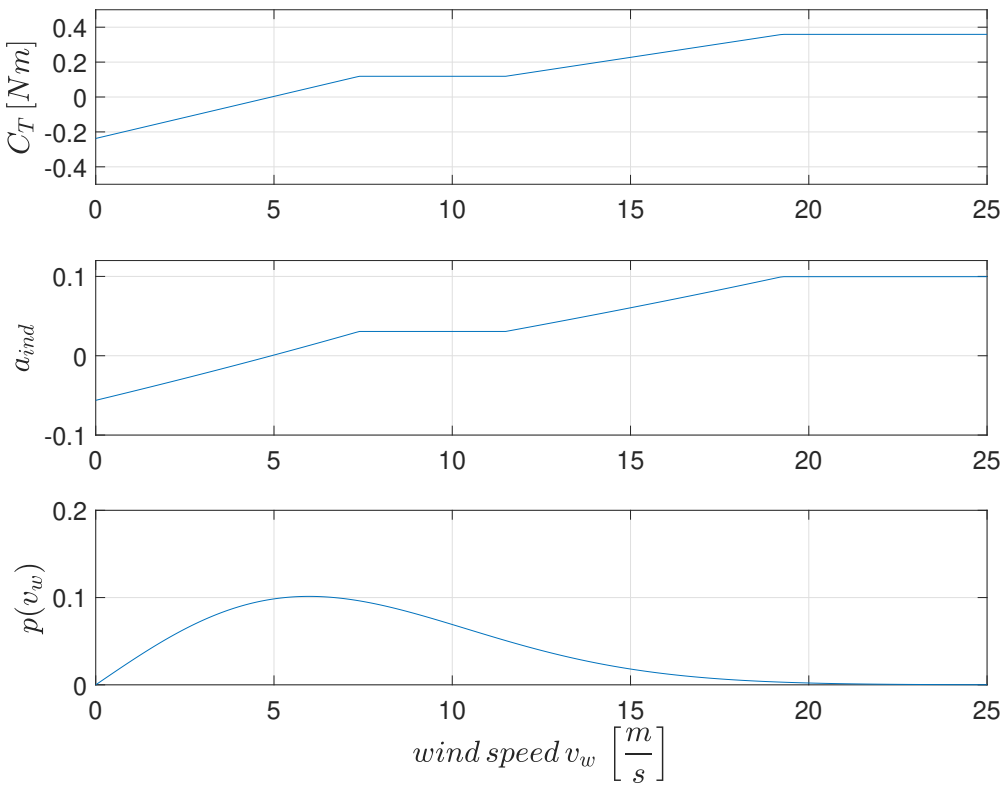


Figure 5.11: Thrust coefficient $C_T$ and axial induction factor $a_{ind}$ plotted over the wind speed $v_w$ and rated over the probability distribution $p(v_w)$.

### 5.4.3 Angle of Attack

The angle of attack $\alpha$ seen by a radial airfoil section of a blade is calculated by the tangential and axial inflow velocity, cleared with the corresponding tangential and axial induction factors, and the local twist of the blade. The lift polar of a NACA0010 airfoil is shown in Fig. 4.5. The lift coefficient $C_l$ increases with the angle of attack from $C_{l,min}(\alpha = 10°) \approx -1$ to $C_{l,max}(\alpha = 10°) \approx 1$. The values $C_{l,min}$ and $C_{l,max}$ additionally limit the scope where stall not occurs. The lift polar was calculated for a Reynolds number of $Re = 2 \cdot 10^5$. With an increasing Reynolds number the NACA0010 airfoil is able to reach higher slightly values for $C_{l,max}$ and $C_{l,min}$ at higher angles of attack without reaching stall. As the range of Reynolds number for the designed rotor is slightly higher than $Re = 2 \cdot 10^5$, the lift polar in Fig. 4.5 fulfills the requirements to perform an exemplary comparison with the angles of attack at the radial blade sections.

The outer part of a blade produces the main torque to transform energy. Therefore, Fig. 5.12 shows the angles of attack at two radial sections with $r_1 = 60\,\%\,R_{tip}$ and $r_2 = 90\,\%\,R_{tip}$ for the whole wind speed scope. The transition point from motor- in generator mode is still located at $v_w \approx 5\,\frac{m}{s}$.

A negative angle of attack indicates that the corresponding section supplies thrust for motor mode, a positive angle of attack supplies thrust for generator mode. As seen in Fig. 5.12 the section $r_1$ at 60 % of the radius never supplies thrust for the motor mode. The whole thrust for the motor mode is supplied by the sections close to the blade tip. This corresponds with the assumption that the most work is done by the outer sections. Not only do they provide the thrust for the motor mode, they also have to compensate the smaller amount of generator thrust supplied by the inner sections. The angles of attack are low in motor mode. This corresponds with the low thrust coefficients $C_T$ what the rotor has to supply in motor mode. The shape of

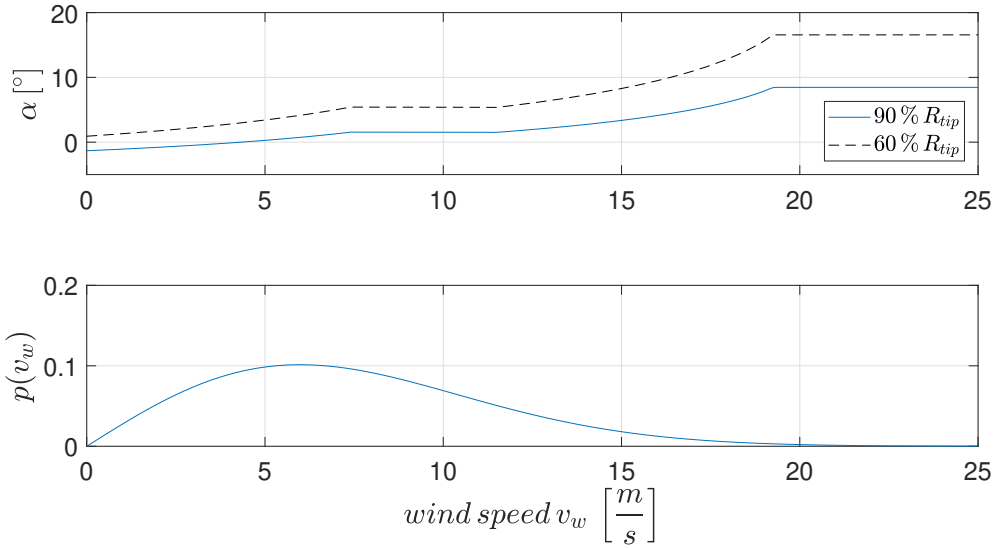


Figure 5.12: Angle of attack $\alpha$ at two radial positions with $r_1 = 60\,\%\,R_{tip}$ and $r_2 = 90\,\%\,R_{tip}$ plotted over the wind speed $v_w$ and rated over the probability distribution $p(v_w)$.

the outer section 2 confirms the location of the transition point because the angle of attack is $\alpha = 0$ for $v_w \approx 5\,\frac{m}{s}$, and therefore symmetric airfoil does not produce thrust.

As mentioned before, the outer sections are dominant and need to be focused in detail. For the whole scope of wind speeds, the angle of attack of section 2 is permanently below $\alpha < 9°$. The stall region starts at $\alpha_{stall} \approx 10°$. Hence, the outer sections, especially the blade tip, never reaches the stall region. The inner sections support the outer section by working at an angle of attack of $\alpha \approx 5°$ at the main focused wind speed of $7\,\frac{m}{s} < v_w < 12\,\frac{m}{s}$. Therefore, the inner sections are working in the scope where a NACA0010 airfoil reaches the highest efficiency, shown in Fig. 4.8a. The optimization made a tradeoff between not reaching stall at the outer meaningful sections and still supply thrust at high wind speed, and maximizing the power output for the wind speeds with a high probability. The thrust supplied by the outer sections at high wind speeds is powerful enough to neglect the stalling inner sections.

### 5.4.4 Airfoil Selection

The optimization revealed that a symmetric NACA0010 airfoil at the hub, the mid, and the tip of the blade reaches the highest efficiency. To analyze these results, the optimized airfoil is compared to other feasible NACA 4 digit airfoils inside the bounds of the optimization. The comparison is distinguished in two figures. Fig. 5.13 compares the optimized symmetric airfoil to the same airfoil with a higher thickness, the NACA0014. Fig. 5.14 shows the comparison to a asymmetric cambered airfoil, the NACA2410. Each figure shows a subfigure for the shape of the airfoils, the lift-to-drag ratio, the lift polar, and the drag polar.

The thickness of the optimized NACA0010 is given by the last two of the four digits, and therefore given with 10 % of the chord length. According to this, the NACA0014 has a thickness of 14 %. This can be seen in Fig. 5.13a. The increase in the airfoil thickness keeps the flow over the airfoil longer attached. Slightly higher values for $C_{l,max}$ and $C_{l,min}$ are possible at slightly higher angles of attack (Fig. 5.13c). The drag polar shows a higher drag for the thicker airfoil in the scope of $-0.45 < C_l < 0.45$. Outside this scope the drag of the thinner airfoil is higher. The relation of the lift to the drag coefficient can be seen in Fig. 5.13b. Corresponding to the drag polar the lift-to-drag ratio reaches higher values with the thinner airfoil at lower angles of attack and lower values at higher angles of attack.

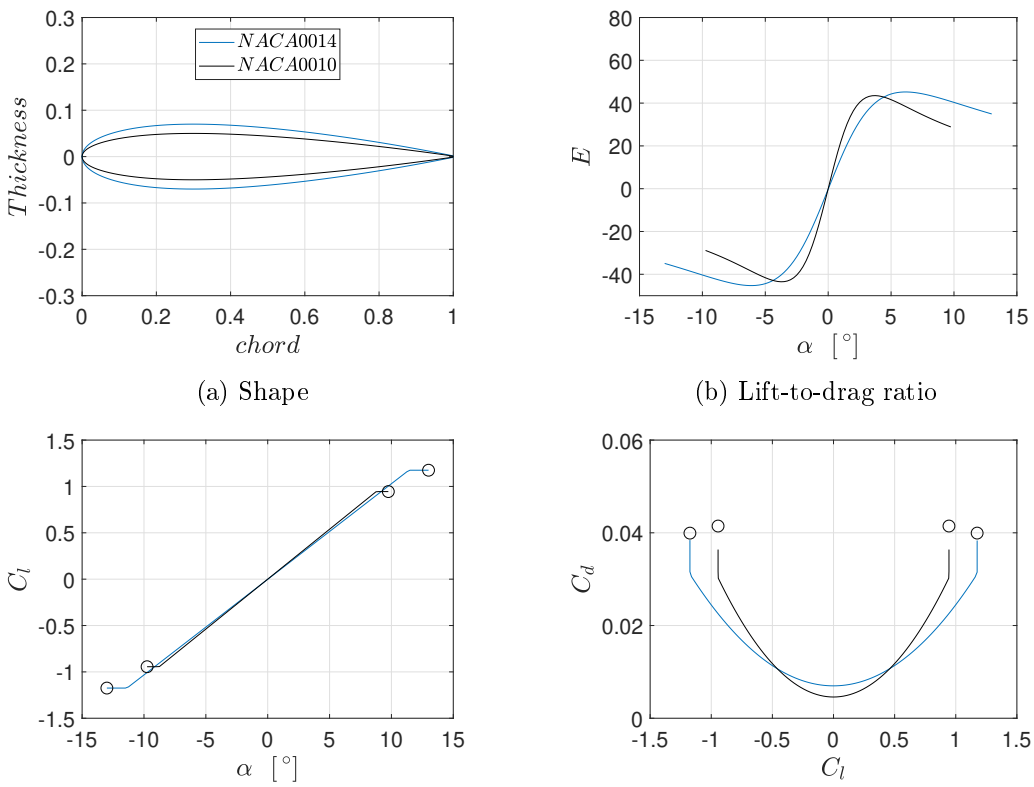


(a) Shape (b) Lift-to-drag ratio

(c) Lift polar (d) Drag polar

Figure 5.13: Symmetric NACA0010 compared to the thicker symmetric NACA0014 with Fig. 5.13a the thickness plotted over the chord, Fig. 5.13b the lift-to-drag ratio $E$ plotted over the angle of attack $\alpha$, Fig. 5.13c the lift coefficient $C_l$ plotted over the angle of attack $\alpha$, and Fig. 5.13d the drag coefficient $C_d$ plotted over the lift coefficient $C_l$.

Thicker airfoils have a bigger resistance surface perpendicular to the axial incoming flow. Therefore, the drag coefficient is higher for low angles of attack. With an increasing angle of attack the deviations between the resistance surface perpendicular to the incoming flow of the thinner and the thicker airfoil gets lower. The nose radius increases with the thickness of the airfoil. A bigger nose radius accelerates the flow around the nose more than a smaller nose radius. Therefore, more energy is saved in the flow over the airfoil and leads to a weaker rise in the drag coefficient at higher angles of attack. Therefore, a thicker airfoil is more efficient at higher angles of attack.

To connect those physical fundamentals to our case, we still need to focus on the meaningful outer sections of the blade. The lift and drag produced at the outer sections is much higher than the lift and drag produced at the inner sections. As shown in Fig. 5.12, the angle of attack at the mainly focused wind speeds of $7\,\frac{m}{s} < v_w < 12\,\frac{m}{s}$ of the outer sections is $\alpha \approx 1.5°$. Hence, the angles of attack are rather low, and therefore thinner airfoils are more efficient.

The shape of the cambered NACA2410 airfoil is shown represented by the blue line in Fig. 5.14a. Cambered airfoils are commonly used in propeller and wind turbine design to increase the efficiency of the system. In general, a cambered airfoil has a higher lift-to-drag ratio than a symmetric airfoil. The same effect as with a thicker nose radius occurs for cambered airfoils. The flow over the airfoil has a longer distance from the leading edge to the trailing edge of the airfoil and needs to accelerate more to reach the leading edge in time. Again, more energy is saved in the flow and a higher pressure jump between the bottom and the top of the airfoil results in a higher lift coefficient (Fig. 5.14c) and a higher lift-to-drag ratio (Fig. 5.14b).

The drag coefficient for low and negative angles of attack of symmetric airfoils are lower than

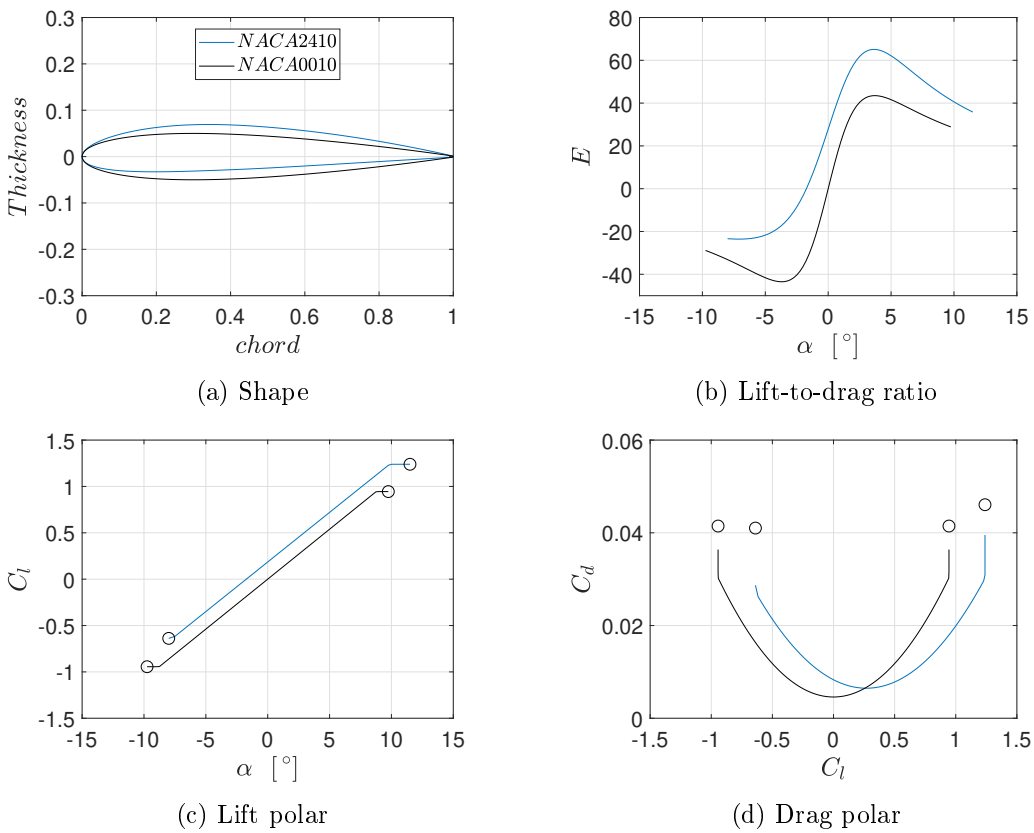


(a) Shape (b) Lift-to-drag ratio

(c) Lift polar (d) Drag polar

Figure 5.14: Symmetric NACA0010 compared to the asymmetric cambered NACA2410 with Fig. 5.14a the thickness plotted over the chord, Fig. 5.14b the lift-to-drag ratio $E$ plotted over the angle of attack $\alpha$, Fig. 5.14c the lift coefficient $C_l$ plotted over the angle of attack $\alpha$, and Fig. 5.14d the drag coefficient $C_d$ plotted over the lift coefficient $C_l$.

the drag coefficients of cambered airfoils (Fig. 5.14d). For higher angles of attack the opposite can be observed, and cambered airfoils increase the efficiency. Cambered airfoils are installed in reverse as they would be for a classical airplane propeller with the aim to support the generator mode. However, aligned with the supporting of the generator mode, cambered airfoils have a negative influence on the efficiency in motor mode.

A comparison between the optimized rotor with the symmetric NACA0010 airfoils and a second optimization, which is limited to only use cambered airfoils, is shown in Fig. 5.15. The rotor efficiency $\eta$ is plotted for both rotors over the wind speed $v_w$ and rated over the probability distribution $p(v_w)$. The efficiency of the rotor with the symmetric airfoils is higher in both modes. The deviation between the efficiencies is increasing towards the transition point from motor in generator mode. This behavior confirms the assumptions that symmetric airfoils at low angles of attack and for lightly loaded rotors are more efficient.

As the angles of attack at the mainly focused wind speed is low, and the rotor also has to supply thrust in motor mode, CMA-ES yields symmetric airfoils for the whole blade to increase the efficiency.

### 5.4.5 Power Harvesting Factor

The power harvesting factor $\zeta$ is defined in Eq. 3.22. It compares the total amount of energy in the wind with the aerodynamic power $P_a$ and is used as a dimensionless comparative factor for AWESs. Fig. 5.16 shows the shape of the power harvesting factor plotted over the wind speed $v_w$. The power harvesting factor is only meaningful for energy systems working in generator-mode,

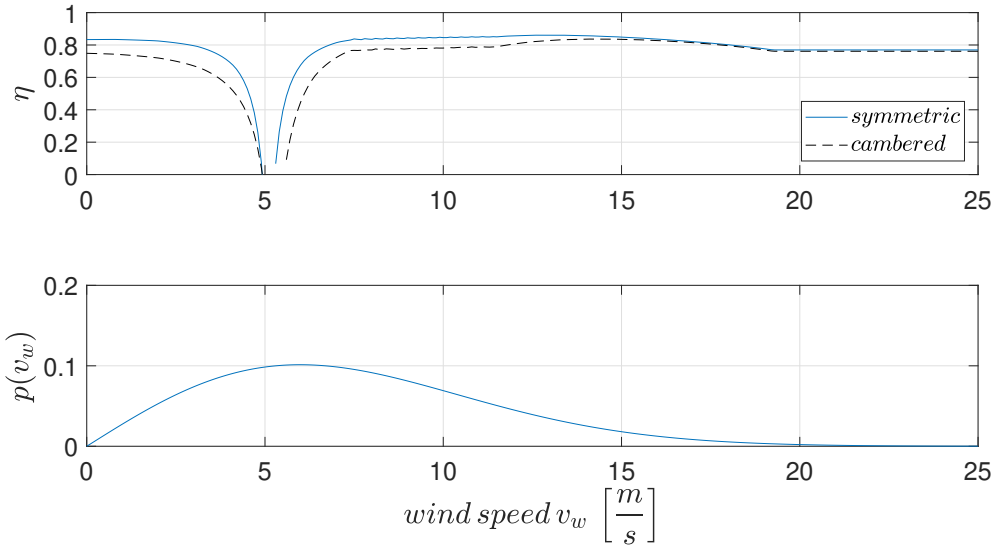


Figure 5.15: Rotor efficiency $\eta$ plotted over the wind speed $v_w$ and rated over the probability distribution $p(v_w)$ for the optimized rotor with symmetric airfoils and another optimized rotor with only cambered airfoils.

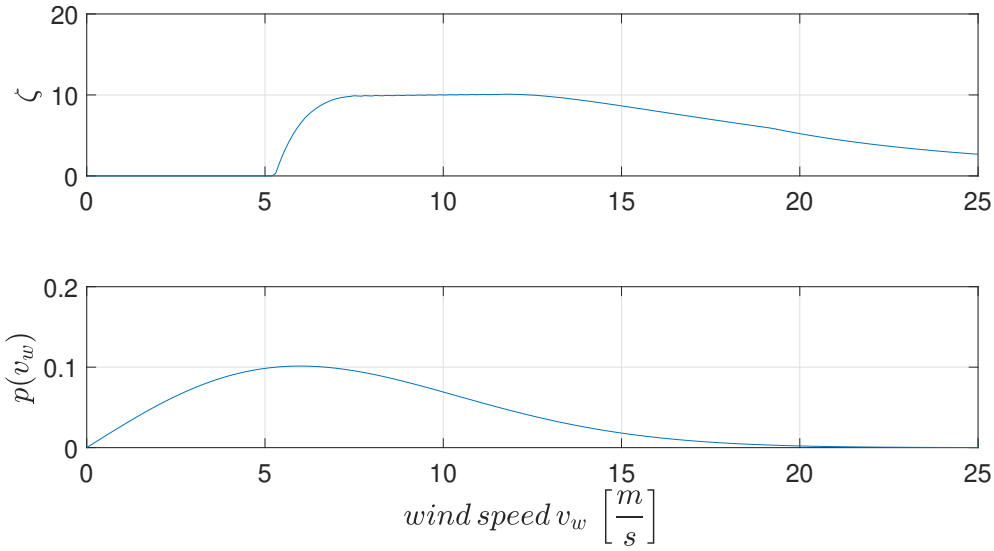


Figure 5.16: Power harvesting factor $\zeta$ plotted over the wind speed $v_w$ and rated over the probability distribution $p(v_w)$.

and is therefore $\zeta = 0$ for $v_w < 5.5\,\frac{m}{s}$. The maximum of shape is located in the scope of the main focused wind speed of $7\,\frac{m}{s} < v_w < 12\,\frac{m}{s}$ and reaches a value of $\zeta = 10$. For higher wind speed, the factor decreases approximately linear.

Chapter 6

# Conclusion and Outlook

The coupling of the interactive rotor design program XRotor and the genetic algorithm CMA-ES turned out to be a powerful tool to optimize a multi-objective rotor design for a wide scope of wind speeds. To find the global optimum, the chord distribution, the twist distribution, and the blade shape have been regulated by the evolutionary algorithm. The result is a highly efficient rotor, which has been optimized with the lifting line theory of XRotor, based on the bound vortex and the helicoidal wake, and confirmed by the BEMT (Fig. 5.8).

A detailed analysis showed that the Mach number at the blade tip is low in all flight configurations and the Reynolds number (Fig. 5.10) is almost constant in radial direction. Stall is avoided at the considerable outer sections of the blade due to low angles of attack (Fig. 5.12). Furthermore, the optimized symmetric airfoils have been compared to an independent optimization limited to cambered airfoils (Sec. 5.4.4), which showed that the symmetric airfoils achieved higher efficiencies. Three independent optimizations with a three-bladed, a five-bladed, and a seven-bladed rotor have been performed. The five-bladed rotor provided the highest annual energy yield with the deviations being vanishingly low.

The rotor design procedure in the present work can be adapted to any drag power kite operating at different locations with individual wind conditions.

Based on the present work, several subsequent topics concerning the current rotor design emerged:

- **Computational Fluid Dynamics:** To further verify the optimized rotor a CFD-analysis is recommendable. A first approach could be the coupling of the reynolds-averaged navier-stokes equations (RANS) with the BEMT according to [33]. The coupling with the BEMT could reduce the computational efforts to a fraction.

- **Noise emission:** At early stages small-scale drag power kites operate close to inhabited areas. The noise emission of a rotor increases with the rotational speed and the loading of the rotor as the blade tip vortices are getting stronger. To predict reliable noise levels, further investigation is needed. XRotor is able to calculate the noise emissions of a given rotor design.

- **Finite-Element-Method:** A structural analysis of the designed rotor is mandatory. A structural fail of a rotor during crosswind flight or hover could cause a collapse of the complete system and result in a crash. Therefore, a FEM-analyze needs to be performed before manufacturing the rotors.

- **Experimental investigations:** The inflow velocities of the rotor disc area are relatively low and are in the scope of the wind tunnels installed at the aerodynamic chair of the Technical University of Munich. Therefore, it seems useful to perform wind tunnel tests as part of a scientific paper which compares the performed experimental data with the results of the optimization.

[1] Uwe Ahrens, Moritz Diehl, and Roland Schmehl. *Airborne wind energy*. Springer Science & Business Media, 2013.

[2] *Ampyx Power B.V.* (accessed Juni 12, 2019). URL: https://www.ampyxpower.com/.

[3] Anne Auger and Nikolaus Hansen. "A restart CMA evolution strategy with increasing population size". In: *2005 IEEE congress on evolutionary computation*. Vol. 2. IEEE. 2005, pp. 1769–1776.

[4] Florian Bauer. "Multidisciplinary Optimization of Drag Power Kites". unpublished Dissertation. Technical University of Munich, 2018.

[5] Florian Bauer et al. "Drag power kite with very high lift coefficient". In: *Renewable energy* 118 (2018), pp. 290–305.

[6] Nicholas K Borer and Mark D Moore. "Integrated propeller-wing design exploration for distributed propulsion concepts". In: *53rd AIAA Aerospace Sciences Meeting*. 2015, p. 1672.

[7] Tony Burton, David Sharpe, and Nick Jenkins. *Handbook of wind energy*. John Wiley & Sons, 2001.

[8] Antonello Cherubini et al. "Airborne Wind Energy Systems: A review of the technologies". In: *Renewable and Sustainable Energy Reviews* 51 (2015), pp. 1461–1476.

[9] Anthony Colozza. "High altitude propeller design and analysis overview". In: *Federal Data Systems Cleveland Ohio* 44135 (1998).

[10] M Drela and H Youngren. "XROTOR: an interactive program for the design and analysis of ducted and free-tip propellers and windmills, 2011.[Software]". In: *Public/web/xrotor/[Accessed 15 November 2012]* ().

[11] Mark Drela. "XFOIL: An analysis and design system for low Reynolds number airfoils". In: *Low Reynolds number aerodynamics*. Springer, 1989, pp. 1–12.

[12] Mark Drela and Harold Youngren. *XROTOR user guide*. 2003.

[13] William Frederick Durand. *Aerodynamic Theory: A General Review of Progress Under a Grant of the Guggenheim Fund for the Promotion of Aeronautics*. Springer-Verlag, 2013.

[14] *EnerKíte - Flugwindkraftanlagen*. (accessed Juni 12, 2019). URL: https://www.enerkite.de/.

[15] Lorenzo Fagiano and Mario Milanese. "Airborne wind energy: an overview". In: *2012 American Control Conference (ACC)*. IEEE. 2012, pp. 3132–3143.

[16] H Glauert. "Aerodynamic theory". In: *The Aeronautical Journal* 34.233 (1930), pp. 409–414.

[17] Sydney Goldstein. "On the vortex theory of screw propellers". In: *Proceedings of the Royal Society of London. Series A, Containing Papers of a Mathematical and Physical Character* 123.792 (1929), pp. 440–465.

[18] Nikolaus Hansen. "The CMA evolution strategy: a comparing review". In: *Towards a new evolutionary computation*. Springer, 2006, pp. 75–102.

[19] Nikolaus Hansen. "The CMA evolution strategy: A tutorial". In: *arXiv preprint arXiv: 1604.00772* (2016).

[20] Alexander Hirner et al. "Improvement of Propulsive Efficiency by Dedicated Stern Thruster Design". In: *7th AIAA ATIO Conf, 2nd CEIAT Int'l Conf on Innov and Integr in Aero Sciences, 17th LTA Systems Tech Conf; followed by 2nd TEOS Forum*. 2007, p. 7702.

[21] Bryce Humpert, Richard Gaeta, and Jamey D Jacob. "Optimal Propeller Design for Quiet Aircraft using Numerical Analysis". In: *21st AIAA/CEAS Aeroacoustics Conference*. 2015, p. 2360.

[22] Th von Karman. "Compressibility effects in aerodynamics". In: *Journal of the Aeronautical Sciences* 8.9 (1941), pp. 337–356.

[23] *Kitepower. Delft University of Technology, Section Wind Energy, Faculty of Aerospace Engineering*. (accessed Juni 12, 2019). URL: https://kitepower.nl/.

[24] E Eugene Larrabee and Susan E French. "Minimum induced loss windmills and propellers". In: *Journal of Wind Engineering and Industrial Aerodynamics* 15.1-3 (1983), pp. 317–327.

[25] Miles L Loyd. "Crosswind kite power (for large-scale wind power production)". In: *Journal of energy* 4.3 (1980), pp. 106–111.

[26] *Makani Technologies*. (accessed Juni 12, 2019). URL: https://makanipower.com/.

[27] George Pocock. *The Aeropleustic Art Or Navigation in the Air, by the Use of Kites Or Buoyant Sails*. Sherwood & Company, 1827.

[28] Ludwig Prandtl and Albert Betz. *Vier Abhandlungen zur Hydrodynamik und Aerodynamik*. Vol. 3. Universitätsverlag Göttingen, 2010.

[29] Volker Quaschning. *Regenerative Energiesysteme: Technologie-Berechnung-Simulation*. Carl Hanser Verlag GmbH Co KG, 2015.

[30] Hermann Schlichting and Erich A Truckenbrodt. *Aerodynamik des Flugzeuges: Erster Band: Grundlagen aus der Strömungstechnik Aerodynamik des Tragflügels*. Springer-Verlag, 2013.

[31] Johan BHM Schulten. "Advanced propeller performance calculation by a lifting surface method". In: *Journal of propulsion and power* 12.3 (1996), pp. 477–485.

[32] Tomas Sinnige and Leo L Veldhuis. "Pylon trailing edge blowing effects on the performance and noise production of a pusher propeller". In: *52nd Aerospace Sciences Meeting*. 2014, p. 0566.

[33] M Stuhlpfarrer, A Valero-Andreu, and C Breitsamter. "Numerical and experimental investigations of the propeller characteristics of an electrically powered ultralight aircraft". In: *CEAS Aeronautical Journal* 8.3 (2017), pp. 441–460.

[34] Yorick Teeuwen. "Propeller Design for Conceptual Turboprop Aircraft". In: (2017).

[35] *The CMA Evolution Strategy*. 2007 (accessed Juni 12, 2019). URL: http://cma.gforge.inria.fr/.

[36] Theodore Theodorsen. *Theory of propellers*. McGraw-Hill Book Company, 1948.

[37] *TwingTec AG*. (accessed Juni 12, 2019). URL: http://twingtec.ch/de/.

[38] *University of Freiburg. syscop. Systems Control and Optimization Laboratory, IMTEK, Faculty of Engineering, University of Freiburg*. (accessed Juni 12, 2019). URL: https://www.syscop.de/.

[39] Nando Van Arnhem. "Design and Analysis of an Installed Pusher Propeller with Boundary Layer Inflow". In: (2015).

[40] Kianoosh Yousefi and Alireza Razeghi. "Determination of the critical Reynolds number for flow over symmetric NACA airfoils". In: *2018 AIAA Aerospace Sciences Meeting*. 2018, p. 0818.